Austrian Journal of Earth Sciences | Vienna | 2016 | Volume 109/2 | 211 - 232 | DOI: 10.17738/ajes.2016.0016

Microbially-driven formation of Cenozoic siderite and calcite concretions from eastern Austria

Lydia M. F. BAUMANN[1),2)*)], Daniel BIRGEL[1)], Michael WAGREICH[2)] & Jörn PECKMANN[1),2)];

[1)] Institut für Geologie, Universität Hamburg, Bundesstraße 55, 20146 Hamburg, Germany;

[2)] Department für Geodynamik und Sedimentologie, Universität Wien, Althanstraße 14, 1090 Wien, Austria;

[*)] Corresponding author: lydia.baumann@uni-hamburg.de

KEYWORDS concretions; Cenozoic; siderite; calcite

Abstract

Carbonate concretions from two distinct settings have been studied for their petrography, carbon and oxygen stable isotope patterns, and lipid biomarker inventories. Siderite concretions are enclosed in a Paleocene-Eocene deep-marine succession with sandy to silty turbidites and marl layers from the Gosau Basin of Gams in northern Styria. Septarian calcite concretions of the southern Vienna Basin from the sandpit of Steinbrunn (Burgenland) are embedded in Upper Miocene brackish sediments, represented by calcareous sands, silts, and clays. Neither for the siderite, nor for the calcite concretions a petrographic, mineralogical, or stable isotope trend from the center to the margin of the concretions was observed, implying that the concretions grew pervasively. The $\delta^{13}C$ values of the Gams siderite concretions (-11.1 to -7.5‰) point to microbial respiration of organic carbon and the $\delta^{18}O$ values (-3.5 to +2.2‰) are in accordance with a marine depositional environment. The low $\delta^{13}C$ values (-6.8 to -4.2‰) of the Steinbrunn calcite concretions most likely reflect a combination of bacterial organic matter oxidation and input of marine biodetrital carbonate. The corresponding $\delta^{18}O$ values (-8.8 to -7.9‰) agree with carbonate precipitation in a meteoric environment or fractionation in the course of bacterial sulfate reduction. Lipid biomarkers have been extracted before and after decalcification of the concretions in order to assess pristine signatures and to exclude secondary contamination. The siderite concretions did not yield indigenous biomarkers due to their high thermal maturity. The calcite concretions comprise abundant plant wax-derived long-chain *n*-alkanes, reflecting high terrestrial input. Bacterial-derived, terminally-branched fatty acids and hopanoids were found, but with overall low contents. The presence of framboidal pyrite, the moderately low $\delta^{13}C$ values, and the biomarker inventory indicate that bacterial sulfate reduction contributed to the formation of the calcite concretions in a brackish environment. The low $\delta^{13}C$ values of the siderite concretions, on the other hand, are best explained by bacterial iron reduction, since sulfate reduction and resultant hydrogen sulfide production would have inhibited siderite precipitation. This study documents a new example for an exception from the common pattern that siderite concretions preferentially precipitate in freshwater environments. The Gams siderite concretions formed within marine sediments, whereas the Steinbrunn calcite concretions formed in freshwater to brackish sediments.

Karbonatkonkretionen aus verschiedenen Ablagerungsräumen wurden im Hinblick auf ihre Petrografie, stabile Kohlenstoff- und Sauerstoffisotope und Lipidbiomarkerinhalt untersucht. Sideritkonkretionen entstammen paleozän-eozänen, tiefmarinen, sandigen bis schluffigen Turbiditen und Mergellagen des Gosaubeckens von Gams in der nördlichen Steiermark. Septarische Kalzitkonkretionen des südlichen Wiener Beckens aus der Sandgrube von Steinbrunn (Burgenland) sind eingebettet in obermiozäne, brackische Sedimente, die durch teilweise bituminöse, kalkige Sande, Schluffe und Tone repräsentiert werden. Weder für die Siderit- noch für die Kalzitkonkretionen konnten petrografische oder mineralogische Trends, noch Trends in der Verteilung stabiler Isotope vom Zentrum zum Rand beobachtet werden, was auf ein gleichmäßiges und ungerichtetes Wachstum der Konkretionen hindeutet. Die $\delta^{13}C$-Werte des Siderits (-11.1 bis -7.5‰) weisen auf mikrobielle Umsetzung von organischem Kohlenstoff hin und die $\delta^{18}O$-Werte (-3.5 bis +2.2‰) sind im Einklang mit einem marinen Sedimentationsraum. Die $\delta^{13}C$-Werte des Gosausediments deuten auf einen marinen Ursprung des Karbonats hin, während die Sauerstoffisotope am besten mit einer meteorischen Überprägung erklärt werden können. Die $\delta^{13}C$-Werte der Kalzitkonkretionen (-6.8 bis -4.2‰) spiegeln höchstwahrscheinlich eine Mischung von Karbonat aus bakterieller Oxidation von organischer Substanz mit marinem, biodetritärem Karbonat wieder. Die $\delta^{18}O$-Werte reichen von -8.8 bis -7.9‰, was in Übereinstimmung mit der Bildung in einer meteorischen Umgebung ist, aber auch auf Fraktionierung im Zuge von bakterieller Sulfatreduktion hindeuten kann. Lipidbiomarker wurden vor und nach der Auflösung des Karbonats der Konkretionen extrahiert, um ihre Authentizität zu garantieren und um rezente Oberflächenkontamination auszuschließen. Die Sideritkonkretionen enthalten aufgrund ihrer hohen thermischen Reife keine Biomarker aus dem ehemaligen Ablagerungsraum mehr. Die Kalzitkonkretionen enthalten von Pflanzenwachsen stammende, langkettige *n*-Alkane, die Eintrag von terrestrischen Blattwachsen repräsentieren. Bakterielle molekulare Fossilien, wie zum Beispiel endverzweigte Fettsäuren und Hopanoide wurden gefunden, allerdings mit geringen Gehalten. Nichtsdestotrotz deuten diese Biomarker, zusammen mit dem Vorkommen von framboidalem Pyrit und den moderat niedrigen $\delta^{13}C$-Werten auf die Rolle von Sulfatreduktion bei der Konkretionsbildung hin. Fortwährende Sulfatreduktion

und die daraus resultierende Produktion von Schwefelwasserstoff inhibieren die Fällung von Siderit. Daher können die niedrigen $\delta^{13}C$-Werte der Sideritkonkretionen am besten durch bakterielle Eisenreduktion erklärt werden. Diese Studie liefert ein weiteres Beispiel für eine Abweichung von der allgemeinen Annahme, dass sich Sideritkonkretionen bevorzugt in Süßwassermilieus bilden. Tatsächlich haben sich die untersuchten Sideritkonkretionen in marinen Sedimenten gebildet, wohingegen die Kalzitkonkretionen unter Süß- bis Brackwasserbedingungen gewachsen sind.

1. Introduction

Concretions are confined bodies of clastic sediment lithified by authigenic minerals. They form during shallow burial of sediments, preferably within the first tens of meters when the surrounding sediment is still unconsolidated, and are, thus, products of early diagenesis (Blome and Albert, 1985; Pye et al., 1990; Mozley, 1996; Raiswell and Fisher, 2004). Sellés-Martínez (1996) provided an elaborate classification scheme of various concretionary bodies, distinguishing between cements, veins, nodules, and concretions. Nodules and concretions are very similar. However, whereas concretions incorporate material of the host sediment, nodules contain solely authigenic phases. Concretions are usually spherical or ellipsoidal, but also come as elongated, oblate, tubular, lobate, or irregular bodies (Coleman and Raiswell, 1995; Duck, 1995; Thomka and Lewis, 2013). The authigenic phases of concretions that cement the background sediment are composed of carbonate, phosphate, silica, sulfide, sulfate, and iron oxide minerals (Coleman et al., 1985; Mozley, 1996; Yli-Hemminki et al., 2014). Most common parageneses are carbonate concretions in clayey or sandy horizons, quartz or chert in limestones, and pyrite in black shales (Coleman et al., 1985; Sellés-Martínez, 1996), and the most common concretion-forming minerals are carbonates such as calcite, Mg-calcite, Fe-calcite, siderite, and dolomite (Siegel et al., 1987; Pye et al., 1990; Mozley, 1996). Concretion size varies from millimeters to meters, and estimated growth rates vary from tens to hundreds up to thousands of years for decimeter-sized concretions (Duck, 1995; Pratt, 2001; Thomka and Lewis, 2013). The growth of concretions of meter size is assumed to take millions of years (Sellés-Martínez, 1996). In great contrast, Pye et al. (1990) described modern siderite concretions up to 40 cm in diameter, which were formed in few decades, because the host sediment, a salt marsh at the north Norfolk coast (UK), has only been deposited since World War II.

Many studies have developed detailed scenarios for the growth of concretions (e.g. Coleman et al., 1985; Mozley, 1996; Raiswell and Fisher, 2000; Loyd et al., 2014). Two opposing scenarios have been put forward, the "concentric growth" and the "pervasive growth" model. During concentric growth, rigid, fully cemented layers are added to the outer surface of the concretion until the final volume is reached only at the end of growth, whereas during pervasive growth, the final volume of the concretion is defined from the onset of cementation and cement crystals grow simultaneously throughout the entire volume. The latter mode appears to produce only poorly lithified concretions (Raiswell and Fisher, 2000). However, a variety of complex intermediate growth modes may occur that fall between the two endmember modes. Most recent studies favor the pervasive growth scenario (e.g. Raiswell and Fisher, 2000; Lash and Blood, 2004; Loyd et al. 2014).

The most common explanation of what is inducing the formation of the authigenic carbonate minerals of carbonate concretions is microbial oxidation of buried organic matter under anoxic conditions (Irwin et al., 1977; Blome and Albert, 1985; Siegel et al., 1987; Mortimer and Coleman, 1997; Kiriakoulakis et al., 2000; Lash and Blood, 2004; Mortimer et al., 2011; Loyd et al., 2012a/b). The main biogeochemical processes that are believed to have the potential to induce carbonate precipitation are (1) dissimilatory ferric iron reduction, (2) bacterial sulfate reduction, and (3) archaeal hydrogenotrophic methanogenesis. These processes can increase the pH or alkalinity. Characteristic isotopic signatures and molecular fossils (lipid biomarkers) of the prokaryotes involved in carbonate formation can be preserved in the carbonate matrix (e.g. Irwin et al., 1977; Coleman et al., 1993; Duan et al., 1996; Pearson et al., 2005; Reitner et al., 2005).

Regardless of the processes triggering cement formation, concretions only form in a confined zone of the sediment column. The equilibrium model suggests that an entire volume of sediment is uniformly supersaturated in carbonate, and concretions form wherever appropriate nuclei are present (Coleman and Raiswell, 1995; Raiswell and Fisher, 2000). However, only few concretions with nuclei have been documented (Pye et al., 1990; Thomka and Lewis, 2013), whereas the majority of concretions lacks nuclei (e.g. Siegel et al., 1987; Kiriakoulakis et al., 2000; Lash and Blood, 2004; Loyd et al., 2012a). An alternative model, the so-called dynamic or local-equilibrium model presumes a spatial variation in carbonate saturation, caused by localized biogeochemical activity, which in turn results from a heterogeneous distribution of organic matter (Coleman et al., 1985; Raiswell and Fisher, 2000). In some cases, where organic matter contents are low (e.g. Lash and Blood, 2004), diffusion and fluid flow are alternative mechanisms for the formation of concretions (fluid-mixing model by Raiswell and Fisher, 2000).

Here, subspherical to elliptical siderite and calcite concretions from two locations in eastern Austria were studied. The host sediment of the studied siderite concretions comprises sandy to silty turbidites in the Gosau Basin of Gams, northern Styria. The basin is part of the Northern Calcareous Alps and belongs to the Upper Gosau Subgroup, which reflects a marine deep water environment around the Paleocene-Eocene boundary, 55 Ma ago (Wagreich et al., 2011). The studied calcite concretions are from the sandpit of Steinbrunn (Čáry Formation) in the southern Vienna Basin, which represents the transition from fully marine to limnic conditions during the Pannonian, around 10 Ma ago (Grundtner et al., 2009). The current work emphasizes on the factors steering growth geo-

metry and the mechanisms of carbonate precipitation. It particularly tries to shed light on the biogeochemical processes and types of prokaryotes involved, looking at the mineralogy, stable isotope composition, and lipid biomarker inventories of the Gams and Steinbrunn concretions.

2. Geological setting

2.1 Gosau Basin of Gams

Sandy to silty, turbidite-dominated deposits with thin layers and concretions of siderite crop out in the basin of Gams, in northern Styria, east of the Enns valley, Northern Calcareous Alps (Figure 1). The section is part of the Zwieselalm Formation of the Upper Gosau Subgroup (Wagreich et al., 2011). The Gosau Group is composed of sediments lying unconformably upon parts of the Calcareous and Central Alps, which suffered extensive folding and thrusting by the Early Cretaceous orogenesis (Faupl and Wagreich, 1996). The sediments were deposited in the northwestern Tethyan realm in a regime formed by transtension and further subsidence. The so-called "Gosau sea" gradually inundated the Austro-Alpine microplate from the north (Faupl and Wagreich, 1996). First, the Northern Calcareous Alps received sediment from the accretionary wedge of the subducting Southern Penninic ocean in the north, as well as the Tethys suture in the south. From the Maastrichtian onwards, sediment delivery changed and the southern metamorphic units of the Austroalpine became the only source region (Stern and Wagreich, 2013). The Gosau Group developed from a subtropical, terrestrial to shallow water environment (Lower Gosau Subgroup) in the Late Turonian to Campanian to a deep water sedimentary environment (Upper Gosau Subgroup) from the Campanian to Ypresian (Faupl and Wagreich, 1996; Wagreich, 2001).

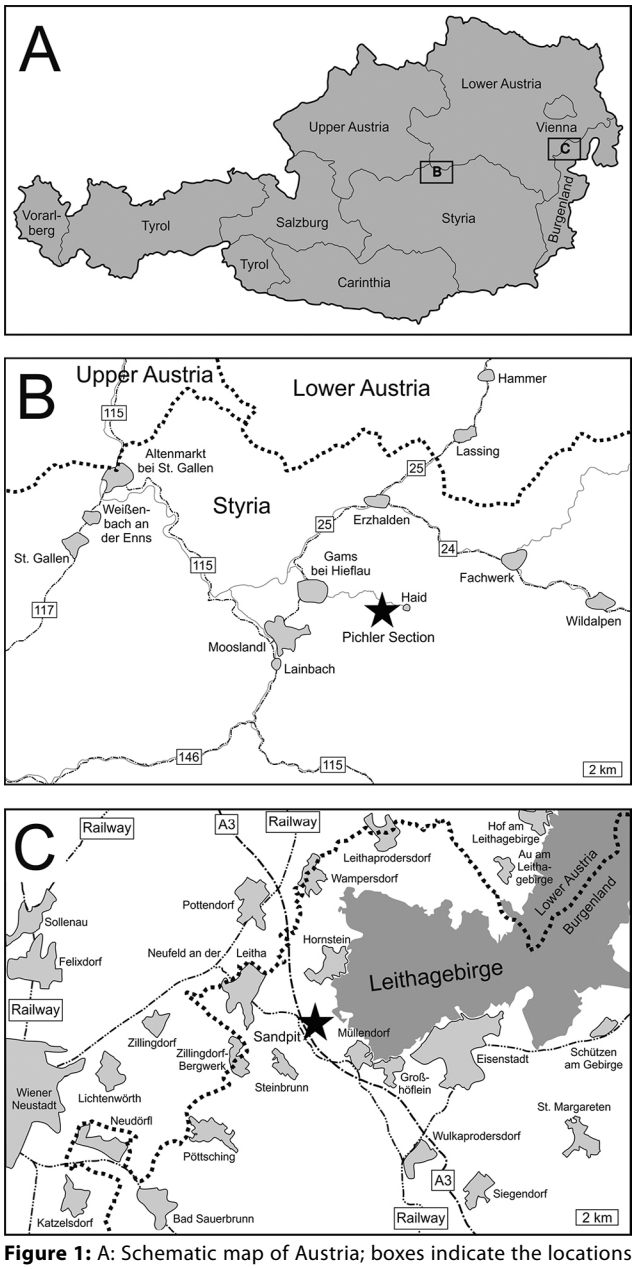

Figure 1: A: Schematic map of Austria; boxes indicate the locations of the detailed maps B and C. B: Location of the investigated section (asterisk) along the flanks of a southern unnamed tributary creek of the Gamsbach. C: Location of the Steinbrunn sandpit (asterisk) at the southwestern edge of the Leithagebirge.

In the Gosau Basin of Gams both the Lower and the Upper Gosau Subgroup are exposed. The Upper Gosau Subgroup is represented by the Nierental and the Zwieselalm Formation (Egger et al., 2004; Wagreich et al., 2011). The Zwieselalm Formation spans from the Danian to the Ypresian, with siderite concretions and layers occurring around the Paleocene-Eocene boundary (55 Ma), ranging from ca. 56 to 54.5 Ma. The Zwieselalm Formation is primarily composed of turbidites, whereas the underlying Nierental Formation (Campanian to Danian) represents a basin slope environment, characterized by pelagic marls and marly limestones with intercalated thin turbidites. The section studied by Wagreich et al. (2011), the so-called Pichler section (014° 50′ 25″ E; 47° 39′ 40″ N), comprises 122 m of the Zwieselalm Formation. The part of the sections with siderite concretions and beds is dominated by psammitic to pelitic turbidites, either carbonate-free or with distinctive marl layers (Figure 2). The siderite concretions are embedded within sandy-silty as well as in silty-clayey material. Among these, dark claystones contain 0 to 6.4 wt. % carbonate (Wagreich et al., 2011). Generally, Wagreich et al. (2011) assumed high sedimentation rates of approximately 20 cm/ka for the turbidite successions.

2.2 Sandpit Steinbrunn

The sandpit of Steinbrunn (Figure 1) in Burgenland close to the border to Lower Austria (016° 25′ 43″ E, 47° 51′ 13″ N) consists of calcareous sands, silts, clays, and detrital limestones of the Vienna Basin and its continuation into the Eisenstadt Basin (Piller et al., 1996; Grundtner, 2009; Grundtner et al., 2009; Wieninger, 2009). The northeast-southwest striking Vienna Basin is a rhomb-shaped pull-apart basin that is about 200 km in length and 50 km in width, located between the Eastern Alps, the Western Carpathians and the Western Pannonian Basin (Piller et al., 1996; Strauss et al., 2006). The basin developed in the Miocene and was filled by sediments of the Central Paratethys Sea, ranging from the Karpatian to the Pannonian (Figure 3).

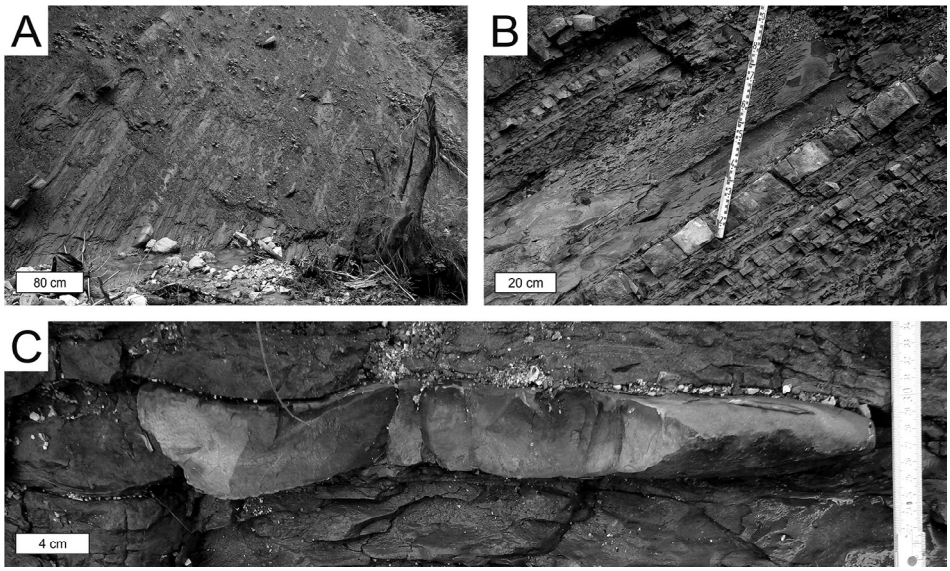

Figure 2: Photographs of the Pichler section (Zwieselalm Fm.). A: Part of the outcrop with well-bedded deep water strata. B: Detailed view of the host rock of the siderite concretions consisting of psammitic to pelitic turbidites with intercalated marl layers. C: Siderite concretion embedded in the host rock.

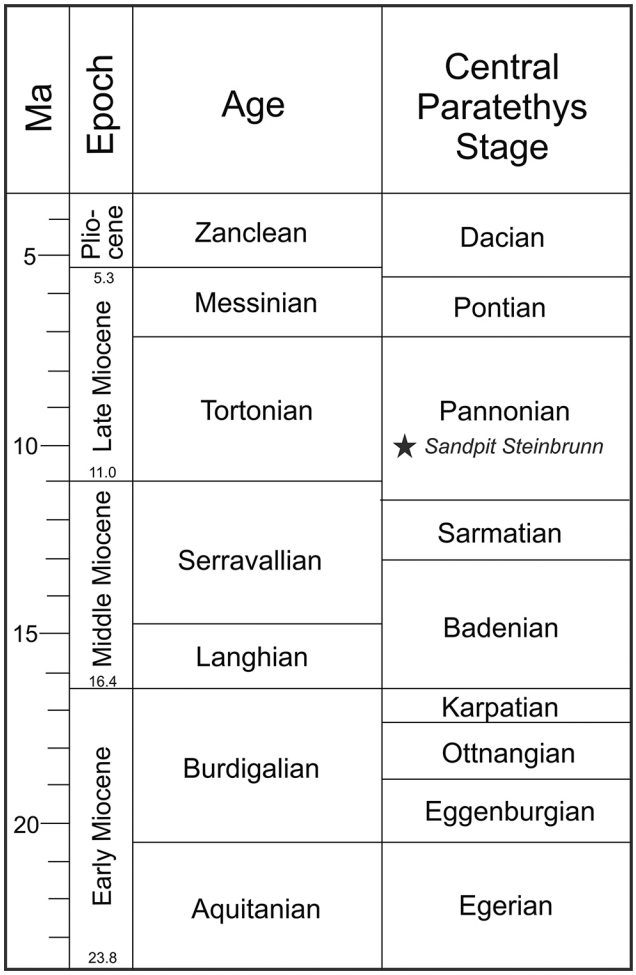

Figure 3: Stages of the Central Paratethys in comparison to global chronostratigraphic chart; modified from Piller et al. (1996).

The sandpit of Steinbrunn comprises largely unconsolidated sediments of Pannonian age (11.6 – 7.1 Ma), belonging to the Lower Neufeld beds or Čáry Formation (Grundtner et al., 2009; Figure 4). While during the Badenian and Sarmatian the Vienna Basin was fully marine, it was consecutively separated from the Paratethys in the Pannonian and transformed into the brackish, later limnic Pannonian Lake (Piller et al., 1996; Grundtner et al., 2009). The Steinbrunn sandpit deposits represent this brackish-limnic stage, but also contain reworked, detrital marine limestones of the Badenian, so-called "Leithakalk" with abundant remnants of coralinaceans and bryozoans. The strata of the sandpit, ranging in age from ca. 10.1 to 9.9 Ma, show a coarsening and shallowing upward trend (Grundtner et al., 2009). The lowermost section, called unit A, comprises 6 m of laminated clays and silts with carbonate contents around 20 wt. % (Grundtner et al., 2009; Figure 4). Unit A contains chiefly quartz, calcite, dolomite, but also minor feldspar, muscovite, and the clay minerals smectite and chlorite. The clays and silts are light brown to dark gray in color, and contain bitumen. Grundtner et al. (2009) classified the section as deposits of a local brackish-limnic pond. Carbonate concretions were found exclusively in Unit A.

3. Materials and Methods

Three siderite concretions from the Gams locality (GA) and ten calcite concretions from Steinbrunn (ST) plus the respective host rocks were examined. GA-1 is a sample of the host rock of the siderite concretions (Figure 5A; Table 1), GA-2, GA-3 and GA-4 are siderite concretions. Siderite concretions are of platy to rounded shape, but not elongated (Figure 5B-C). The height of the three concretions is 5, 7, and 9 cm, respectively, and the diameter is approximately 16 to 17 cm. ST-11 is a sample of the host rock of the calcite concretions (Figure 6A). Calcite concretions (ST-1 to ST-10) are oblate, sometimes elongated and in one case, dumbbell-shaped, bodies. Their height ranges from 3 to 10 cm, their width from 4 to 20 cm, and their length from 10 to 37.5 cm (Figure 6B-D).

Uncovered thin sections from all siderite concretions, from six calcite concretions, and their host rock were prepared (Table 1) and studied with an optical Leica DM 2700 P microscope using plane-polarized as well as cross-polarized light and the magnifications 25, 100, 200, and 630. Images were taken with this microscope equipped with a Leica MC170 HD camera. To identify the different carbonate minerals, selected thin sections were stained with alizarin red S and potassium ferricyanide as described by Dickson (1965). For quantitative graphic evaluati-

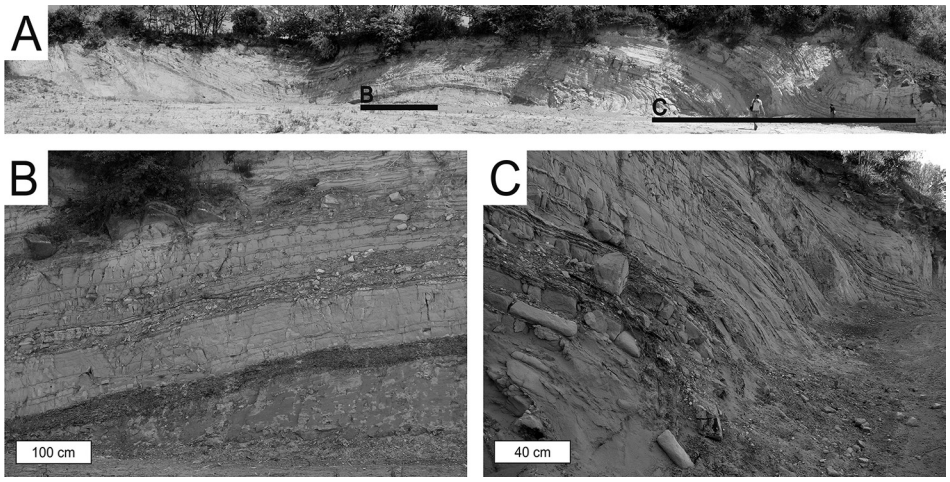

Figure 4: Photographs of the Steinbrunn sandpit. A: Overview of the outcrop; bars indicate the positions of the details figured in B and C. B: Lowermost part of the section with the dark, fine-grained unit A. C: Concretionary layer in the lower left part of the photograph; beds reveal a coarsening upward trend (toward the upper right).

on of carbonate contents from thin section photomicrographs, the image processing and analysis software "ImageJ" was used. The taxonomy of foraminifera follows Rupp (1986) and Loeblich and Tappan (1987).

Carbonate contents (weight %) of all siderite concretions and selected calcite concretions and the host rocks were determined (Table 1), using the carbonate bomb after Müller and Gastner (1971). Per measurement 700 mg of powdered sample, generated with a handheld micro-drill, were dissolved with concentrated hydrochloric acid in a cylindrical jar with a manometer calibrated in percent of calcium carbonate.

Samples for carbon and oxygen stable isotope measurements were taken from slabs of the concretions and the host rock sample ST-11, using a handheld micro-drill (Table 1), and were measured at the University of Graz using the procedure as described in Heindel et al. (2015). The powdered samples were dissolved in 100 % phosphoric acid in a Kiel II automated reaction system at 70°C. The resulting carbon dioxide gas was analyzed in a Finnigan Delta Plus mass spectrometer with a precision better than 0.05‰ for $\delta^{13}C$ and 0.1‰ for $\delta^{18}O$ values. The δ values are corrected according to the NBS19 standard and reported in per mill (‰) relative to the Vienna-PeeDee Belemnite (V-PDB) standard. All $\delta^{13}C$ and $\delta^{18}O$ values mentioned in the text refer to this standard.

The $\delta^{18}O$ values of siderite have been corrected for the sake of comparison with calcite values. The fractionation factors of calcite-water and siderite-water have been calculated using the equation of Zheng (1999):

$$10^3 ln\alpha = A \times 10^6/T^2 + B \times 10^3/T + C$$

First, the A, B and C values for calcite-water were used, and the second time the equivalent values for siderite-water were used:

	A	*B*	*C*
calcite-water	*4.01*	*-4.66*	*1.71*
siderite-water	*4.23*	*-4.58*	*1.73*

Having calculated two different fractionation factors, one for calcite-water and one for siderite-water, the difference between the two fractionation factors was calculated and this value was subtracted from each of the $\delta^{18}O$ values of siderite. As there is very little fractionation of carbon isotopes during precipitation and dissolution reactions (Loyd et al., 2014), no correction of $\delta^{13}C$ values was made.

The method used for extracting lipid biomarkers from calcite and siderite concretions (Table 1) is similar to the method introduced by Birgel et al. (2006), which is a modified method as introduced by Bligh and Dyer (1959). Further, an extraction-decalcification-extraction procedure as introduced by Arning et al. (2009) for phosphorites was applied.

Nr.	Name	Locality and type	Thin section	Carbonate content	Isotopes	Biomarker
1	GA-1	Gams host rock		34		
2	GA-2	Gams concretion	Yes/stained	72.5	6 (profile)	Yes
3	GA-3	Gams concretion	Yes/stained	80	2	
4	GA-4	Gams concretion	Yes	81.5	2	Yes
5	ST-1	Steinbrunn concretion				
6	ST-2	Steinbrunn concretion				
7	ST-3	Steinbrunn concretion	Yes/stained	86	2	
8	ST-4	Steinbrunn concretion	Yes	86	2	Yes
9	ST-5	Steinbrunn concretion	Yes/stained	84	5 (profile)	
10	ST-6	Steinbrunn concretion		85.5		
11	ST-7	Steinbrunn concretion	Yes/stained	85.5	2	
12	ST-8	Steinbrunn concretion	Yes		2	
13	ST-9	Steinbrunn concretion				
14	ST-10	Steinbrunn concretion	Yes		2	Yes
15	ST-11	Steinbrunn host rock	Yes/stained	83.5	4 (profile)	

Table 1: List of all samples. "Yes" = thin section was made/lipid biomarkers were analyzed; carbonate contents are given in % according to the results obtained with the Müller-Gastner Bombe or thin section graphical analysis; numbers in the "Isotopes" column are numbers of subsamples taken.

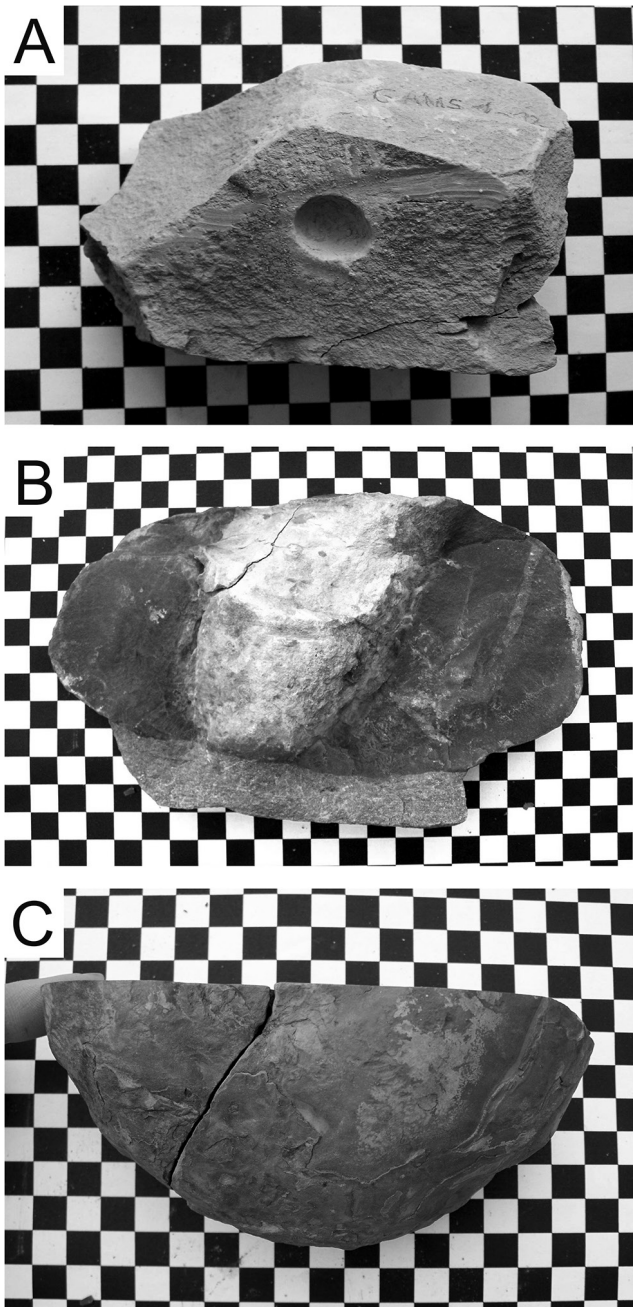

Figure 5: Photographs of Gams siderite concretions and their host rock. One square equals one square centimeter. The large hole marks the sites from which material for carbonate analysis was removed. A: Host rock GA-1. B: Cross section through siderite concretion GA-3 with gray host rock at the bottom. Note the softer core (light). C: Exterior view of one half of siderite concretion GA-4.

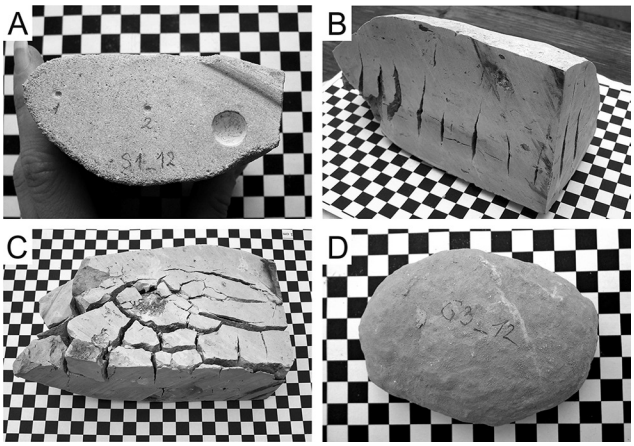

Figure 6: Photographs of selected Steinbrunn calcite concretions and their host rock. One square equals one square centimeter. A: Host rock ST-11; the two small holes are the spots where material for isotope analysis was taken, the large hole marks the site where material for carbonate content analysis was removed. B: Calcite concretion ST-10 cut along two vertical sections; note sub-vertically oriented septarian cracks. C: Horizontal section of calcite concretion ST-10; polygonal crack pattern and cracks parallel to elongation. D: Exterior view of calcite concretion ST-9.

The material was first cleaned with *n*-hexane (SupraSolv® for GC-ECD/FID; Merck Millipore) and dichloromethane (DCM, EMSURE®, ACS, ISO, Reag. Ph. Eur. for analysis; Merck Millipore) to exclude contaminations on the surfaces. Then the sample was broken up with a hammer and powdered with a mortar, respectively. 100 g of rock for each sample was powdered on average. For quantification, three internal standards were added, 5-α-cholestane for hydrocarbons, 1-nonadecanol for alcohols, and 2-methyl-C_{18} fatty acid for the fatty acid fraction. The powdered samples were mixed with an organic solvent mixture (DCM: methanol 3:1; methanol SupraSolv® for GC; Merck Millipore) to extract the organic compounds. The organic solvent mixture was separated from the powder by centrifugation and was decanted and collected in a separatory funnel. This procedure was repeated two to three times, at least until the extract became colorless. The pooled lipid extracts were treated with deionized, DCM-cleaned water and then separated into an organic and an aqueous phase. The organic phase was dried with sodium sulfate in a funnel and then reduced in the rotation evaporator to receive a dry total lipid extract. This first extraction procedure contains those biomarkers, which are not tightly bound to the carbonate matrix. The extracted carbonate powder was dissolved with 10 % hydrochloric acid (diluted from 32 % hydrochloric acid; Merck Millipore) to aim for compounds enclosed within the carbonate matrix. Calcite was dissolved at room temperature, whereas siderite was dissolved at 47°C. After digesting the carbonate until ca. 80 % of the carbonate was dissolved, the solution was centrifuged and the supernatants were decanted and discarded as explained above. The resulting solid material was then saponified to release fatty acids, and after that, the supernatants of this saponification were collected in a separatory funnel. The residual powder after decalcification and saponification was extracted with the same solvent mixture as above and the resulting, extracted organic compounds were added to the supernatants of the saponification. Again, the pooled extracts were cleaned with water, but 10 % hydrochloric acid was further added until pH = 2 was reached, to release the fatty acids from the aqueous phase into the organic phase.

The DCM soluble asphaltenes were separated from the *n*-hexane soluble maltenes to receive cleaner extracts and a better separation and less background on the gas chromatograph. The maltenes were further separated by solid-phase column chromatography, with an SPE-aminopropyl silica gel column (6 ml

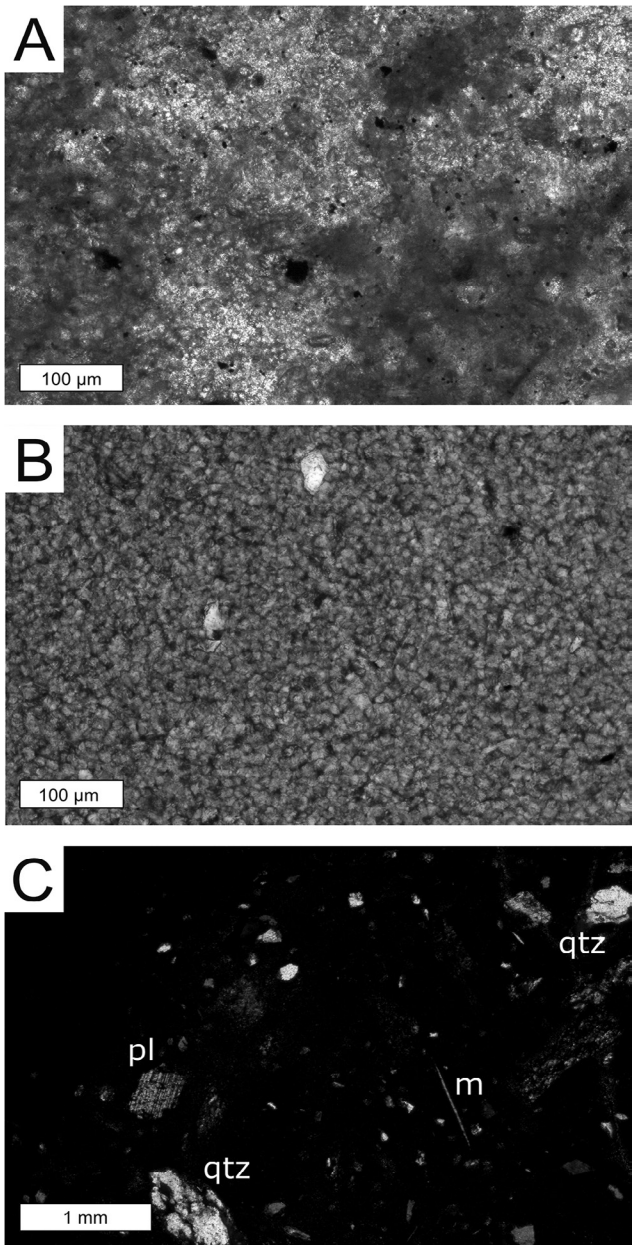

Figure 7: Photomicrographs of Gams siderite concretions. A, B: Siderite concretions GA-3 (A) and GA-2 (B, stained thin section), saccharoidal siderite microspar with few detrital minerals (dark); plane-polarized light. C: Siderite concretion GA-3, plagioclase with polysynthetic twinning (pl), polycrystalline quartz with oscillatory extinction (qtz), and mica (m) in a matrix of siderite microspar (dark); cross-polarized light.

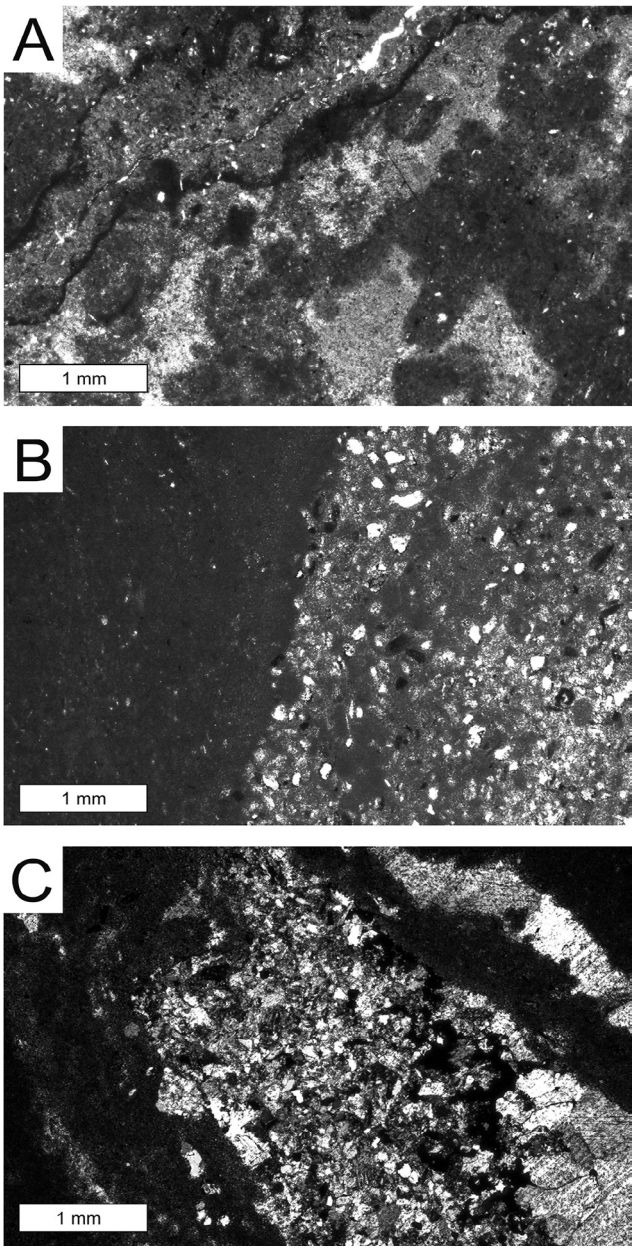

Figure 8: Photomicrographs of Gams siderite concretions. A: Siderite concretion GA-3, patchy appearance caused by changes in carbonate content; plane-polarized light. B: Siderite concretion GA-3, concretion body mainly composed of siderite (left) and siliciclastic sediment (right); plane-polarized light. C: Siderite concretion GA-4, crack through concretion filled with coarse sparry calcite (light) and xenomorphic and partially euhedral quartz (yellow); cross-polarized light.

Glass Tube W/Teflon Frits 500 mg DSC-NH2; Supelco). By using solvents with increasing polarity, the total extracts were divided into four fractions: hydrocarbons (4 ml *n*-hexane), ketones (6 ml *n*-hexane:DCM 3:1), alcohols (7 ml DCM:acetone 9:1), and fatty acids (8 ml 2% formic acid in DCM). Compounds in the alcohol fraction were derivatized to trimethylsilyl ethers by reacting with bis(trimethylsilyl)-trifluoroacetamide (Fluka; Sigma-Aldrich) and pyridine (Merck Millipore). Fatty acid fraction compounds were derivatized to fatty acid methyl esters with boron trifluoride (Fluka). Since the ketone and alcohol fractions did not contain pristine compounds, they are not discussed below.

Measurements were carried out using a gas chromatograph equipped with a flame ionization detector (GC-FID), an Agilent 7820 A GC system, for quantification. For identification, all samples were measured on a GC linked to a quadrupole mass spectrometer (GC-MS), an Agilent 7890 A GC system coupled to an Agilent 5975 C inert MSD mass spectrometer. Both GC-FID and GC-MS used helium as carrier gas and were equipped with a 30 m HP-5 MS UI fused silica capillary column (0.25 mm in diameter, 0.25 µm film thickness). The GC temperature program was as follows: 60 °C (1 min); from 60 °C to 150 °C at 10 °C/min; from 150 °C to 320 °C at 4 °C/min, 25 min isothermal

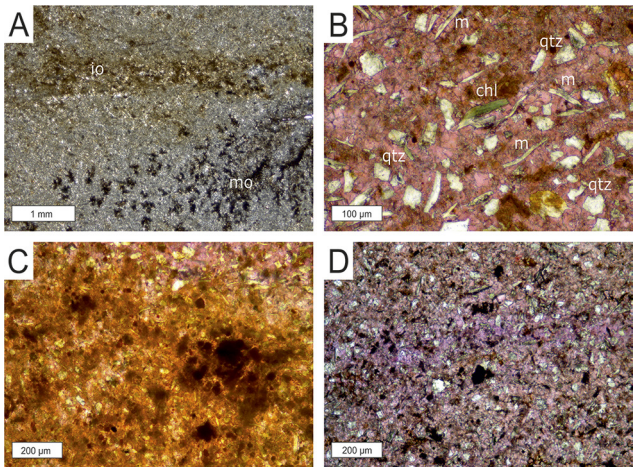

Figure 9: Photomicrographs of Steinbrunn calcite concretions; pink: calcite; purple: ferroan calcite; white: detrital quartz, mica, and authigenic dolomite; black: iron oxyhydroxides or pyrite; reddish brown: oxidation rims of opaque minerals; chl: chlorite; io: iron oxyhydroxides; m: mica; mo: dendritic manganese oxides; pl: plagioclase; qtz: quartz. A: Calcite concretion ST-7; plane-polarized light. B: Calcite concretion ST-5; stained thin section, plane-polarized light. C: Calcite concretion ST-7, oxidized zone with abundant iron oxyhydroxides, probably oxidized pyrite, and authigenic dolomite; stained thin section, plane-polarized light. D: Calcite concretion ST-5, band of ferroan calcite from the left to the right; stained thin section, plane-polarized light.

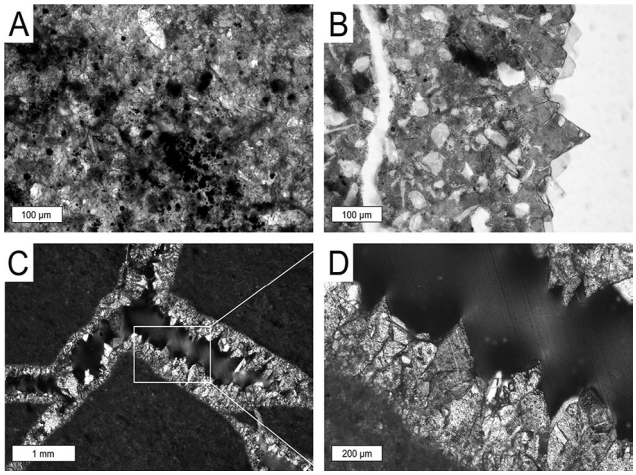

Figure 10: Photomicrographs of Steinbrunn calcite concretions. A: Calcite concretion ST-5, partially oxidized framboidal pyrite (black); stained thin section, plane-polarized light. B: Crack wall of calcite concretion ST-3 with dog-tooth cement; stained thin section, plane-polarized light. C: Calcite concretion ST-3, septarian crack partially filled with dog-tooth cement; cross-polarized light. D: Enlarged section of C; dog-tooth cement in higher magnification.

for all fractions. Interpretation of gas chromatograms was made with "Agilent MSD Productivity ChemStation for GC and GC/MS Systems Data Analysis Application" software. Quantification of compounds was done by comparing peak areas with the internal standards added before extraction, whereas identification was based on retention times and comparison with the NIST database and published spectra, available in Agilent ChemStation software and in the literature.

For further characterization of *n*-alkane patterns, three parameters describing the distribution of *n*-alkanes were calculated (cf. Kiriakoulakis et al., 2000; El-Shafeiy et al., 2014). The carbon preference index (CPI) describes the freshness of long-chain *n*-alkanes and *n*-fatty acids by comparing the amounts of odd- and even-numbered carbon chains (e.g., Peters et al., 2005 and references therein). For hydrocarbons the odd-numbered *n*-alkanes C_{25} and C_{27} are divided over the even-numbered *n*-alkanes C_{26} and C_{28}. The CPI of fatty acids was calculated by dividing even-numbered straight-chain fatty acids C_{26} and C_{28} over odd-numbered C_{25} and C_{27}. The ratio of short- to long-chain hydrocarbons is expressed as LMW/HMW (Low Molecular Weight/High Molecular Weight). The cut-off is placed between C_{24} and C_{25}, because this better accords with the findings of Eglinton et al. (1962) regarding the comparison of marine vs. terrestrial (leaf waxes) inputs. The LMW/HMW of fatty acids was calculated in the same way as for hydrocarbons by dividing amounts of short-chain fatty acids up to C_{24} over long-chain fatty acids above C_{25}. The Terrestrial-Aquatic Ratio (TAR) was used by Bourbonniere and Meyers (1996) to determine the terrestrial vs. aquatic sources of hydrocarbons and fatty acids. The TAR of hydrocarbons is defined as the ratio between the sum of *n*-C_{27}, *n*-C_{29}, and *n*-C_{31} and the sum of *n*-C_{15}, *n*-C_{17}, and *n*-C_{19}. The long-chain components represent terrestrial

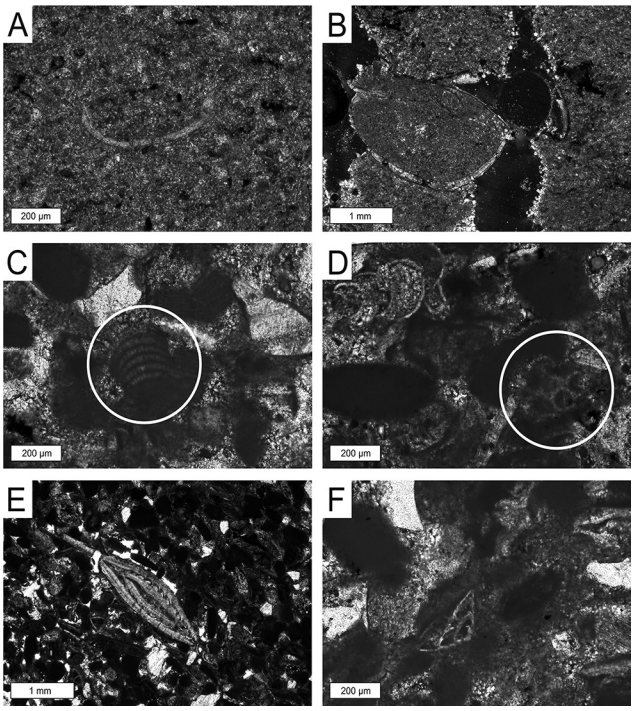

Figure 11: Photomicrographs of Steinbrunn calcite concretions and their host rock. A: Calcite concretion ST-5, probable carapace of an ostracode or a small bivalve; plane-polarized light. B: Calcite concretion ST-3, large ostracod carapace filled with concretionary material in the center; cross-polarized light. C: Calcareous sandstone ST-11, white circle: corallinacean algae; plane-polarized light. D: Calcareous sandstone ST-11, foraminifer (*Bulimina* sp.) in the upper left corner; white circle: bryozoan fragment; plane-polarized light. E: Calcareous sandstone ST-11, foraminifer (*Operculina* sp.) in the center; black: fragments of corallinacean algae; white: detrital minerals; plane-polarized light. F: Calcareous sandstone ST-11, foraminifer (*Rosalina* sp.) in the center; plane-polarized light.

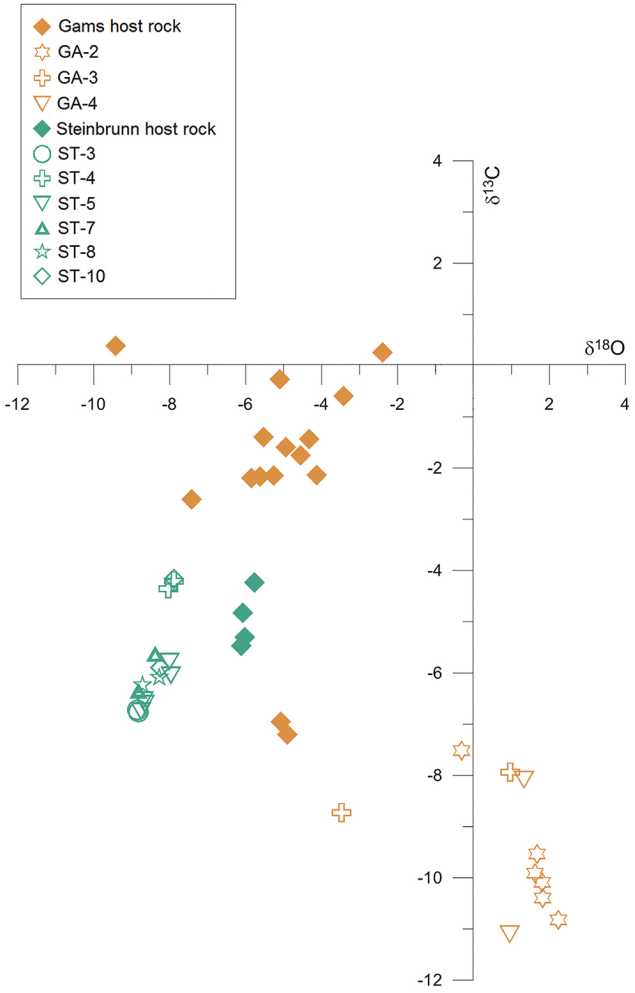

Figure 12: Crossplot of $\delta^{18}O$ against $\delta^{13}C$ values of calcite concretions ST-3, ST-4, ST-5, ST-7, ST-8, and ST-10 and their host rock (ST-11), and all siderite concretions (GA-2, GA-3, GA-4) and their host rock. Values are given in per mill relative to the V-PDB standard.

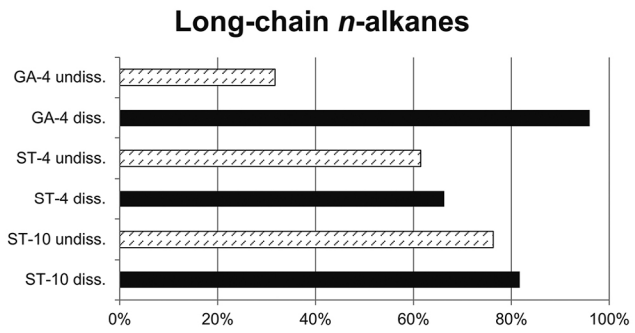

Figure 13: Relative percentages of long-chain *n*-alkanes (of all hydrocarbons detected) in all samples. "undiss." or hatched bar = extract before decalcification; "diss." or filled bar = extract after decalcification.

sources and the short-chain components aquatic sources. It must be taken into account that land-derived organic matter primarily contains higher proportions of *n*-alkanes than aquatic algae. The *n*-alkanes derived from algae are mainly degradation products of fatty acids. Accordingly, especially in fresh samples the TAR may be biased and may overrepresent terrestrial input (Bourbonniere and Meyers, 1996). Due to a lack of components in some of the samples it was not always possible to calculate this ratio. The TAR of fatty acids was calculated by dividing $\Sigma C_{24}+C_{26}+C_{28}$ over $\Sigma C_{12}+C_{14}+C_{16}$ (cf., Bourbonniere and Meyers, 1996; El-Shafeiy et al., 2014).

4. Results

4.1 Macroscopic description, petrography, and carbonate content

4.1.1 Gams siderite concretions

The host sediment of the siderite concretions is a grayish to yellowish mudstone (Figure 5A). The Gams concretions are of reddish brown, rusty color, and lighter and darker zones caused by bioturbation occur. GA-3, for example, has a paler and softer core (Figure 5B), which also reveals a lower carbonate content of 45 %. In contrast, the intact outer part of concretion GA-3 has a carbonate content of ca. 80 % (Table 1). The carbonate content of the concretions is 70 wt. % on average as opposed to 34 wt. % for the host rock (Table 1). No fossils have been found in the concretions. The concretions consist of siderite microspar (Figure 7A and 8A). However, also zones of coarse sparry siderite have been found and the cements occasionally appear saccharoidal (Figure 7A and 7B). Apart from siderite, concretions contain significant amounts of ferroan calcite. The two phases are clearly distinguishable in stained thin sections, where siderite appears light brown, whereas the ferroan calcite is blue. Ferroan calcite fills the residual pore volume between the siderite crystallites. Therefore, siderite predates the formation of ferroan calcite. Detrital minerals enclosed in the siderite concretions are quartz (Figure 8B), plagioclase (Figure 7C), muscovite (Figure 7C), biotite, chlorite, and kaolinite. Quartz is in parts polycrystalline and shows undulose extinction, the typical features of metamorphic quartz (Figure 7C). Nevertheless, also monocrystalline quartz with straight extinction (Figure 8C) was found, implying mixed sources. Siderite concretions reveal a very heterogeneous distribution of siderite cement and siliciclastic material (Figure 8B), coming along with a variation in color from dark brown to light orange (Figure 8A), which is apparently enhanced by bioturbation and fluctuations in carbonate content. Bioturbation is even macroscopically visible, appearing as darker regions and as poorly oriented lenses of coarser-grained siliciclastic material, which are most likely infillings of burrows (Figure 8B).

4.1.2 Steinbrunn calcite concretions

The color of the Steinbrunn calcite concretions is mostly light yellowish brown to gray with red brown patches of iron oxyhydroxides. The host sediment is slightly darker and consists of yellowish silt and clay and fine sand (Figure 6A). A conspicuous feature of all calcite concretions are septarian cracks. The septarian cracks are not filled, but some show small rim cements on crack walls. Orientation of cracks is dominantly vertical (Figure 6B). Horizontal sections show a polygonal pattern in

Hydrocarbons	GA-4		ST-4		ST-10	
Compound	% undiss.	% diss.	% undiss.	% diss.	% undiss.	% diss.
Short-chain *n*-alkanes (<C_{19})	24.9	0.1	8.7	8.1	4 .5	n.d.
Mid-chain *n*-alkanes (C_{19}-C_{24})	46.4	3.9	22.1	19.1	15.2	14.2
Long-chain *n*-alkanes (>C_{24})	26.3	96.0	61.5	66.3	76.3	81.7
C_{27}-hopene	n.d.	n.d.	0.3	0.1	n.d.	n.d.
ββ C_{27}-hopane	n.d.	n.d.	1.0	0.8	1.0	0.7
αβ C_{29}-hopane	0.5	n.d.	0.2	0.4	0.1	0.3
Hop-17(21)-ene	n.d.	n.d.	0.5	0.6	0.3	0.6
βα C_{29}-hopane	n.d.	n.d.	0.1	0.2	0.3	0.5
αβ C_{30}-hopane	0.6.	n.d.	0.3	0.2	0.4	0.4.
ββ C_{29}-hopane	0.3	n.d.	1.0	0.8	0.8	0.3
αβ C_{31}-hopane	0.3	n.d.	0.1	0.2	0.1	0.5
βα C_{31}-hopane	0.6	n.d.	0.3	0.4	0.4	0.6
ββ C_{30}-hopane	n.d.	n.d.	0.3	0.4	0.3.	n.d.
ββ C_{31}-hopane	0.1	n.d.	0.3	0.3	0.2	n.d.
Total *n*-alkanes	97.6	100.0	92.2	93.5	96.0	95.9
Total hopanes	2.4	n.d.	4.6	4.2	4.0	4.1
Pristane + phytane*	n.d.	n.d.	3.2	2.3	n.d.	n.d.

Table 2: Relative percentages of hydrocarbons; undiss. = extract before decalcification; diss. = extract after decalcification; n.d. = not detected; *Coeluting with cycloalkanes, pristane potentially with 1,5-dimethylheptylbenzene and phytane with 1,5-dimethyloctylbenzene or 1,5,9-trimethylnonylbenzene.

Hydrocarbons	GA-4		ST-4		ST-10	
	undiss.	diss.	undiss.	diss.	undiss.	diss.
CPI	1.26	0.82	1.99	2.06	2.24	1.97
LMW/HMW	2.71	0.04	0.50	0.41	0.26	0.17
TAR	0.54	n.c.	4.11	5.36	10.64	n.c.

Table 3: Selected parameters of alkane distributions; CPI = $(C_{25}+C_{27})/(C_{26}+C_{28})$; LMW/HMW: sum of *n*-alkanes ≤ C_{24} divided over sum of *n*-alkanes ≥ C_{25}; TAR = $(C_{27}+C_{29}+C_{31})/(C_{15}+C_{17}+C_{19})$. "undiss." = extract before decalcification; "diss." = extract after decalcification; n.c. = not calculated.

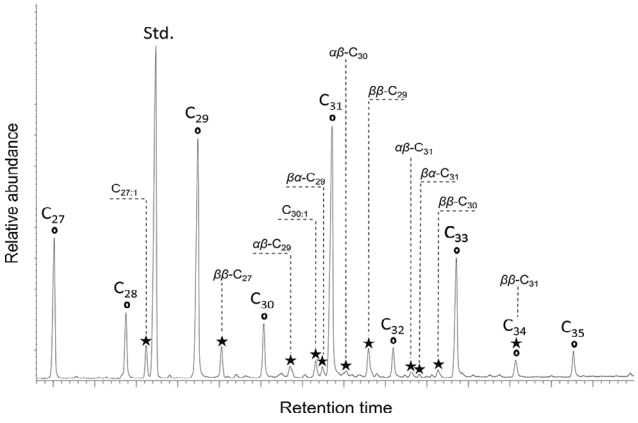

Figure 14: Partial gas chromatogram (total ion current) of the hydrocarbon fraction of ST-4 before decalcification, from *n*-C_{27} to *n*-C_{35}. Std.: standard, 5α-cholestane; circles: *n*-alkanes; stars: hopanes; $C_{27:1}$ = C_{27}-hopene; ββ-C_{27} = ββ C_{27}-hopane; αβ-C_{29} = αβ C_{29}-hopane; $C_{30:1}$ = hop-17(21)-ene; βα-C_{29} = βα C_{29}-hopane; αβ-C_{30} = αβ C_{30}-hopane; ββ-C_{29} = ββ C_{29}-hopane; αβ-C_{31} = αβ C_{31}-hopane; βα-C_{31} = βα C_{31}-hopane; ββ C_{30} = ββ C_{30}-hopane; ββ-C_{31} = ββ C_{31}-hopane.

the center and a preferred orientation along the length of the concretion (Figure 6C). Septarian cracks are widest in the center, and narrowing towards concretion margins. The crack tips commonly do not reach the surface. According to Astin (1986), this crack pattern is quite common for concretions with such a regular shape. Interestingly, the darker and grayer specimen ST-5 contains more pyrite than the other calcite concretions from which thin sections were made (see below). Calcite concretions reach calcite contents of 85 wt.% on average, the host rock contents of ca. 84 wt.% (Table 1) as revealed by carbonate bomb analysis and supported by graphic evaluation of thin section images.

Authigenic minerals cementing the concretions are micrite (i.e. microcrystalline calcite) and sparry calcite, the latter representing so-called microspar (Figure 9A-D). The crystal size distribution is rather heterogeneous and ranges from 5 to 50 µm, a crystal size typical for calcite concretions (Raiswell and Fisher, 2000). It cannot be excluded that parts of the calcite are detrital, which even seems quite likely considering the calcareous nature of the host rock. Beside calcite, the concretions contain quartz, muscovite, chlorite (Figure 9B), plagioclase, K-feldspar, iron oxyhydroxides (Figure 10A), manganese oxides (Figure 9A,C, and 10A), authigenic dolomite (Figure 10B), and fossils. Kerogen or plant debris are common. The iron content is apparently heterogeneous in the concretions, indicated by bands of ferroan calcite (Figure 9D). Pyrite is common and apparently of an authigenic origin based on the framboidal habit of crystal aggregates (Figure 10A). The septarian cracks are mostly unfilled, but many of them reveal beginning cementation by dog-tooth cement (Figure 10B-D).

All concretions and the host rock contain fossils (Figure 11A-F). In the concretions the fossil inventory is dominated by ostracods (Figure 11A). Abundant brownish to yellowish fragments are interpreted as disintegrated ostracods, while other skeletons are still intact, allowing for the confident identification of ostracods (Figure 11B). The most abundant fossils, however, are fragments of corallinacean algae (Figure 11C). Foraminifera, such as *Bulimina* sp., *Rosalina* sp., and *Operculina* sp. are abundant and also bryozoans were observed (Figure 11D-F). Fossils make up more than 50 vol.% of the sandstone, beside them, mineral grains such as quartz (partly polycrystalline), muscovite, kaolinite, and opaque phases were observed.

Fatty acids	GA-4		ST-4		ST-10	
Compound	% undiss.	% diss.	% undiss.	% diss.	% undiss.	% diss.
Short-chain n-fatty acids ($<C_{19}$)	82.9	91.8	76.8	74.2	77.9	74.0
Mid-chain *n*-fatty acids (C_{19}-C_{24})	4.1	2.4	5.8	7.7	6.9	9.4
Long-chain *n*-fatty acids ($>C_{24}$)	0.3	1.1	10.9	6.5	8.4	10.4
iso-$C_{14:0}$	n.d.	n.d.	n.d.	n.d.	n.d.	0.2
iso-$C_{15:0}$	0.2	traces	0.1	0.2	0.1	0.5
anteiso-$C_{15:0}$	0.4	0.1	0.1	0.3	0.1	0.3
iso-$C_{16:0}$	n.d.	0.1	0.1	0.3	0.1	0.2
10Me-$C_{16:0}$	n.d.	n.d.	n.d.	n.d.	n.d.	traces
iso-$C_{17:0}$	0.3	0.2	0.1	0.2	0.1	0.3
anteiso-$C_{17:0}$	0.2	0.3	0.2	0.3	0.2	0.2
αβ C_{31}-hopanoic acid	n.d.	n.d.	n.d.	0.2	traces	0.2
ββ C_{32}-hopenoic acid	n.d.	n.d.	n.d.	0.2	0.1	n.d.
αβ C_{32}-hopanoic acid	n.d.	n.d.	n.d.	0.3	0.5	0.4
ββ C_{31}-hopanoic acid	n.d.	n.d.	0.8	1.0	0.5	0.3
ββ C_{32}-hopanoic acid	n.d.	n.d.	1.5	3.1	1.1	1.2
ββ C_{33}-hopanoic acid	n.d.	n.d.	0.3	0.6	0.2	0.3
Total *n*-fatty acids	87.3	95.3	93.5	88.4	93.3	93.8
Total unsaturated fatty acids	11.6	4.0	3.1	4.5	3.2	1.7
Total branched fatty acids	1.1	0.6	0.6	1.4	0.6	1.4
Total hopanoic acids	n.d.	n.d.	2.9	5.7	2.8	2.5

Table 4: Relative percentages of fatty acids; undiss. = extract before decalcification; diss. = extract after decalcification; n.d. = not detected.

4.2 Stable carbon and oxygen isotopes

$\delta^{13}C$ and $\delta^{18}O$ values of samples of three Gams siderite concretions, as well as six Steinbrunn calcite concretions and their host rock have been measured (Figure 12). Isotope data for the host rock of the siderite concretions were taken from Wagreich et al. (2011). To establish possible concentric trends, samples were taken along profiles from siderite concretion GA-2, calcite concretion ST-5, and its host rock ST-11.

The Gams siderite concretions exhibit a mean $\delta^{13}C$ value of -9.2‰ and a mean $\delta^{18}O$ value of +0.5 %. Their isotopic composition is more heterogeneous than that of the calcite concretions (Figure 12). Sample GA-2, for example, reveals a relatively wide span of $\delta^{13}C$ values from -10.8‰ to -7.5‰. The corresponding $\delta^{18}O$ values range from -0.3‰ to +2.2‰. For both, $\delta^{13}C$ and $\delta^{18}O$ values, no obvious trend from center to margin is apparent. The $\delta^{13}C$ values of the host rock range from -7.2‰ to +0.9‰ and $\delta^{18}O$ values from -9.4‰ to -2.4‰, with an average $\delta^{13}C$ values of -1.9‰ and an average $\delta^{18}O$ values of -5.5‰, and comprise therefore more positive ^{13}C and more negative ^{18}O signatures than the siderite concretions.

The profile of calcite concretion ST-5 revealed variations of ~ 1‰ in $\delta^{13}C$ and $\delta^{18}O$ values between the center and the margins, but lacking a clear trend. The average $\delta^{13}C$ and $\delta^{18}O$ values over the profile (-6.3‰ and -8.4‰) are close to the overall average values of the calcite concretions (-5.8‰ and -8.4‰). The calcite concretion with the lowest ^{13}C and ^{18}O values is ST-3. It reveals a mean $\delta^{13}C$ value of -6.7‰ and a mean $\delta^{18}O$ value of -8.8‰. In contrast, ST-4 shows the highest $\delta^{13}C$ and $\delta^{18}O$ values (-4.3‰ and -8.0‰). The Steinbrunn host rock is slightly enriched in the heavy isotopes with an average $\delta^{13}C$ value of -4.9‰ and average $\delta^{18}O$ value of -6.0‰.

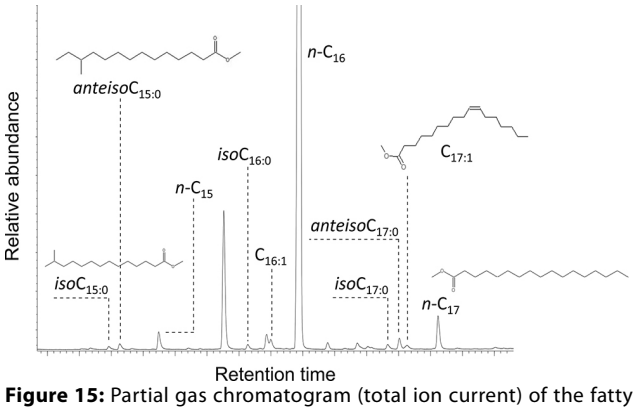

Figure 15: Partial gas chromatogram (total ion current) of the fatty acid fraction of ST-4 after decalcification (measured as fatty acid methyl esters), showing *n*-fatty acids, short-chain, branched and unsaturated fatty acids.

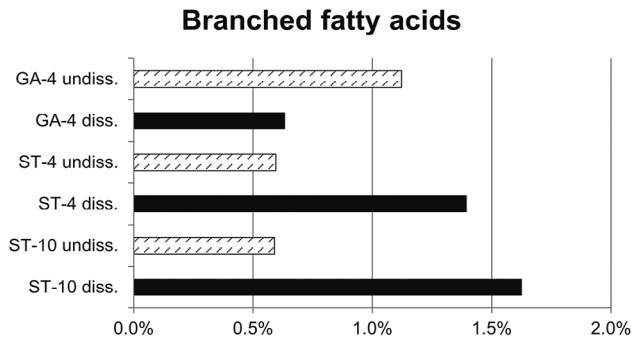

Figure 16: Relative percentages of branched fatty acids (of all fatty acids detected) in all samples. "undiss." or hatched bar = extract before decalcification; "diss." or filled bar = extract after decalcification.

Fatty acids	GA-4		ST-4		ST-10	
	undiss.	diss.	undiss.	diss.	undiss.	diss.
CPI	n.c.	n.c.	1.95	1.95	1.71	1.93
LMW/HMW	288.30	88.88	7.53	12.42	10.07	7.80
TAR	0.02	0.03	0.22	0.19	0.13	0.21

Table 5: Selected parameters of fatty acid distributions; CPI = $(C_{26}+C_{28})/(C_{25}+C_{27})$; LMW/HMW: sum of *n*-fatty acids ≤ C_{24} divided over sum of *n*-fatty acids ≥ C_{25}; TAR = $(C_{24}+C_{26}+C_{28})/(C_{12}+C_{14}+C_{16})$. "undiss." = extract before decalcification; "diss." = extract after decalcification; n.c. = not calculated.

4.3 Lipid biomarker inventory

4.3.1 Hydrocarbons

The hydrocarbon fractions of all concretions in the extracts before and after decalcification predominantly contain *n*-alkanes with chain lengths from 15 to 35 carbon atoms; (Table 2). The siderite concretion GA-4 contains only minor hydrocarbons. The most abundant compound before decalcification is *n*-C_{18}, the least abundant component is *n*-C_{32}. The *n*-alkanes are uniformly distributed before and after decalcification. It has to be noted that GA-4 revealed hydrocarbons with higher carbon numbers in the extract after decalcification, up to *n*-C_{37}. Hydrocarbons of the calcite concretion ST-4 revealed an asymmetrical, bimodal distribution in the extract before decalcification, the two bulges maximize at *n*-C_{19} and *n*-C_{31}. After decalcification, the contents decreased by ca. 50 %. Concretion ST-10 yielded a unimodal hydrocarbon distribution peaking at *n*-C_{31}. Higher contents for hydrocarbons were found after decalcification (Figure 13).

Apart from *n*-alkanes, the isoprenoid hydrocarbons pristane (2,6,10,14-tetramethylpentadecane) and phytane (2,6,10,14-tetramethylhexadecane) were detected in the calcite concretion ST-4 (Table 2), representing 1 % of total hydrocarbons and being slightly less abundant in the decalcified fraction. Nevertheless, their real contents are most likely lower, since they coeluted with cycloalkanes (Table 2).

Siderite concretion GA-4 revealed hopanes only before decalcification (2 %). Eleven hopanes were detected in the hydrocarbon fraction of Steinbrunn concretion ST-4 (Figure 14), ranging from C_{27} (trisnorhopane) to C_{31} (homohopane). Other than saturated hopanes, the monounsaturated hop-17(21)-ene was identified. Interestingly, this compound was found to be more abundant in the extract after decalcification in samples ST-4 and ST-10. ββ C_{29}-Hopane is the second most abundant hopanoid in both calcite concretions, but with lowered content after decalcification.

The siderite concretion GA-4 shows a CPI of around 1, indicating a high maturity. In contrast, the distribution pattern of long-chain *n*-alkanes in the calcite concretions (ST-4 and ST-10) indicates moderate maturation according to the CPI values of around 2 (Table 3). Accordingly, a distinct odd-over-even predominance is still present. The variation in the CPI between the extracts before and after decalcification are only minor (Table 3; Figure 13). The extract of the siderite concretion before decalcification contained three times more LMW than HMW alkanes. In contrast, the extract after decalcification was almost barren of LMW alkanes (LMW/HMW = 0.04).

The Steinbrunn calcite concretions show a very different pattern. The LMW/HMW ratio in calcite concretion ST-4 is similar before and after decalcification (Table 3), with HMW dominating over LMW alkanes by a factor 2. In concretion ST-10, LMW alkanes comprise an even smaller portion of overall alkanes with an LMW/HMW ratio of 0.25 and 0.17 for extracts before and after decalcification, respectively. For the siderite concretion, only the TAR for the fraction before decalcificati-

Short-chain branched and unsaturated fatty acids

Compound	Organisms	References
iso- and *anteiso*-$C_{15:0}$ and -$C_{17:0}$	many bacteria, including SRB	Coleman et al., 1993; Heindel et al., 2012; Guido et al., 2013; Thiel et al., 2014
iso-$C_{16:0}$, *iso*-$C_{18:0}$, *iso*-$C_{19:0}$ and *anteiso*-$C_{19:0}$	unspecified bacteria	Guido et al., 2013
10Me-$C_{16:0}$	SRB (*Desulfobacter* sp.)	Coleman et al., 1993; Duan et al., 1996; Kiriakoulakis et al., 2000; Elvert et al., 2003; Pearson et al., 2005; Heindel et al., 2012; Ziegenbalg et al., 2012; Guido et al., 2013
$C_{16:1\omega5c}$	*Desulfosarcina/Desulfococcus, Desulfotalea, Desulfobulbus* and *Desulforhopalus* sp.	Elvert et al., 2003
$C_{16:1\omega7c}$	*Geobacter* and *Shewanella*	Coleman et al., 1993
iso$C_{17:1\omega7c}$	*Desulfovibrio* sp.	Coleman et al., 1993; Duan et al., 1996; Kiriakoulakis et al., 2000; Elvert et al., 2003; Pearson et al., 2005; Heindel et al., 2012; Ziegenbalg et al., 2012; Guido et al., 2013
$C_{17:1\omega6c}$	*Desulfobulbus, Desulforhabdus* and *Desulforhopalus* sp.	Duan et al., 1996; Elvert et al., 2003

Table 6: Short-chain branched and unsaturated fatty acids, which may serve as biomarkers for different strains of sulfate-reducing bacteria (SRB).

on could have been calculated, resulting in a low ratio of 0.5. The TAR of the calcite concretions is high. ST-4 has a TAR of around 4 before and a TAR of more than 5 after decalcification. This ratio is even higher for ST-10 before decalcification (11).

4.3.2 Fatty acids

The fatty acid fractions of all concretions analyzed are dominated by *n*-fatty acids, ranging from C_{12} to C_{33} and revealing a rather uniform distribution, except for the two most prominent peaks, C_{16} and C_{18}. Most fatty acids are saturated (Table 4), but various unsaturated fatty acids occur, especially in the Gams concretion in the extract before decalcification. This observation and the fact that unsaturated fatty acids are highly unstable, support the view that they are contaminants (summarized as "total unsaturated fatty acids" in Table 4). Beside *n*-fatty acids and unsaturated fatty acids, the siderite concretion is almost barren of lipids in the fatty acid fraction.

Apart from *n*-fatty acids and unsaturated fatty acids, the Steinbrunn calcite concretions contain short-chain, methyl-branched fatty acids, and minor hopanoic acids. In the Steinbrunn concretion ST-10, short-chain, branched fatty acids comprise *iso*-$C_{14:0}$, *iso*-$C_{15:0}$, *anteiso*-$C_{15:0}$, *iso*-$C_{16:0}$, 10Me-$C_{16:0}$, an unidentified branched $C_{16:0}$, *iso*-$C_{17:0}$, and *anteiso*-$C_{17:0}$. *Iso*-$C_{14:0}$ and 10Me-$C_{16:0}$ occur only in the extract after decalcification (Table 4, Figure 15). Branched fatty acids make up 1.1 % (before decalcification) and 0.6 % (after decalcification) in GA-4, 0.6 % (before decalcification) and 1.4 % (after decalcification) in ST-4, and 0.6 % (before decalcification) and 1.6 % (after decalcification) in ST-10 (Figure 16). The siderite concretion thus shows an opposite trend to the calcite concretions. The *anteiso*-$C_{15:0}$ and -$C_{17:0}$ fatty acids are more abundant than the corresponding *iso*-fatty acids in all fractions except for fraction ST-10 after decalcification and GA-4 before decalcification (the latter just for iso and *anteiso*-$C_{17:0}$, Table 4). The most abundant hopanoids in the Steinbrunn concretions ST-4 and ST-10 are ββ C_{31}- and ββ C_{32}-hopanoic acids. Overall, ββ isomers (biohopanoids) predominate over αβ isomers (geohopanoids; cf. Farrimond et al., 2002). No hopanoic acids were detected in the siderite concretion.

The CPIs of the calcite concretions are very similar to those of the hydrocarbon fractions with values from 1.7 to 2.0, indicating moderate maturity (Table 5). Not much difference was observed between the extracts before and after decalcification. For the siderite concretion the CPIs could not be calculated due to the lack of required compounds. The two Steinbrunn samples show an opposite trend in LMW/HMW ratios (Table 5). It is higher after decalcification for ST-4 (8 vs. 12), but lower for ST-10 (10 vs. 8). Extremely high LMW/HMW ratios were calculated for the Gams concretion, 288 (before decalcification) and 89 (after decalcification). Generally, TARs of fatty acids are lower than those of hydrocarbons (Table 5). TARs of the calcite concretions are in the range of 0.1 to 0.2; those of the siderite concretion are even an order of magnitude lower.

5. Discussion

5.1 Reconstruction of the sedimentary environment of the concretion-bearing strata at Steinbrunn

The inventory of the Steinbrunn calcite concretions including abundant corallinacean red algae reveals that many of the detrital components derived from Badenian marine limestones known as "Leithakalk" (cf. Grundtner et al., 2009). It seems likely that the detritus was delivered from the adjacent, elevated area of the Leithagebirge. This scenario is also consistent with the somewhat higher $\delta^{13}C$ value (-4.9‰) of the host sediment compared to the concretions, accounting for a smaller portion of diagenetic carbonate in the host sediment. Similarly, the fact that the calcite concretions reveal somewhat lower $\delta^{18}O$ values than the surrounding sediment could be attributed to the activity of heterotrophic bacteria (e.g. Antler et al., 2013; and chapter 5.4).

Lipid biomarkers help to constrain paleoenvironmental settings (e.g. Brocks et al., 2005). The major difficulty regarding the studied samples from a sandpit affected by weathering is to distinguish between authentic, primary signals and secondary inputs and/or contamination. To exclude secondary signatures and contaminations, an extraction-decalcification-extraction procedure was applied (cf. Arning et al., 2009). As a result of this procedure, the first extract tends to be enriched in compounds that represent secondary input. The compounds of the second extraction after decalcification, which are more tightly bound to the carbonate crystal lattice, are considered to be dominated by pristine biomarkers that are primary components of the sediments or derive from the microorganisms that triggered carbonate formation (Arning et al., 2009; Guido et al., 2013).

The Gams concretions were overprinted in the course of Alpine orogenesis. They reflect high thermal maturity, resulting in the loss of information from lipid biomarkers on the formation environment. Unlike that, low burial depth of the strata bearing the Steinbrunn concretions resulted in good preservation of primary signatures, although ingress of organic molecules at later stages complicated the observed biomarker patterns. The isoprenoids pristane and phytane, for example, are less abundant after decalcification in the calcite concretion ST-4 from the Steinbrunn locality, indicating late stage addition of these compounds. Among others, Rontani and Bonin (2011) reviewed the sources of isoprenoid hydrocarbons in marine environments. They listed chlorophyll and tocopherols (or vitamin E) from cyanobacteria, micro- and macroalgae, and higher plants as well as archaeal lipids (archaeols) as possible sources. However, since archaeal lipids have not been found in any of the siderite and calcite concretions, Archaea are an unlikely source of pristane and phytane in this case. In contrast, there is abundant evidence for significant input of terrestrial, plant-derived detritus, as revealed by the high contents of long-chain *n*-alkanes (cf. Eglinton and Hamilton, 1967). Hence, it is more likely that pristane and phytane derive either from chlorophyll or tocopherols of higher land plants.

Some of the biomarkers in the extracts after decalcification cannot be related to the processes that led to concretion formation, but rather represent remains of organic matter present in the sediment. The calcite concretions formed in a basin, which was characterized by separation from the Paratethys and recurring inflow of freshwater (e.g. Grundtner et al., 2009). Fluviatile transport of terrigenous material into an increasingly brackish pond is in accord with the abundant plant wax-derived long-chain *n*-alkanes in the hydrocarbon fractions of the calcite concretions. Like long-chain *n*-alkanes, long-chain *n*-fatty acids mainly originate from leaf waxes covering and protecting the leaves, stems, flowers, and pollen of higher land plants (Eglinton et al., 1962; Eglinton and Hamilton, 1967; Rommerskirchen et al., 2006). The fact that these land plant biomarkers are particularly abundant in the extract after decalcification confirms that these compounds were primary components of the sediments. These remains of sedimentary organic matter were subsequently incorporated into the calcite concretions, favoring their preservation. The moderate maturity revealed by a calculated CPI of hydrocarbons of approximately two is in good agreement with this hypothesis. Similarly, the almost equal maturities of fatty acids and hydrocarbons is in accord with a common source of these compounds, being intrinsic to the formation environment.

While the components of the Steinbrunn hydrocarbon fractions are mainly of a terrestrial origin, the fatty acid fractions contain a high proportion of short-chain fatty acids, accounting for additional aquatic sources (cf. Bourbonniere and Meyers, 1996; Pearson et al., 2005). This pattern of the Steinbrunn calcite concretions is confirmed by higher TAR and lower LMW/HMW ratios of the hydrocarbon fractions compared to the fatty acid fractions (cf. Bourbonniere and Meyers, 1996). Palmitic (n-$C_{16:0}$) and stearic (n-$C_{18:0}$) acid are the most abundant components in all fatty acid fractions. The high contents of these fatty acids are typical for carbonate concretions (Kiriakoulakis et al., 2000; Pearson et al., 2005), but it is widely accepted that palmitic and stearic acid are ubiquitous in Eukarya and Bacteria, and are therefore unspecific (e.g. Kuechler et al., 2012). In contrast, some short-chain unsaturated fatty acids are specific for certain groups of Bacteria (Table 6). However, double bonds are unstable and the unsaturated fatty acids extracted from the Steinbrunn concretions are thus considered to represent contaminations.

5.2 Concentric vs. pervasive growth

Combined microscopic observations and geochemical results help to constrain the growth mode of the studied concretions. The siderite concretions of Gams (1) lack septarian fractures, (2) reveal no decrease in cement content toward the margin, and (3) show no isotopic trends in profiles from the center to the margin. The latter two observations argue against concentric growth. Further, the siderite concretions consist of two cements throughout the concretion bodies, which are siderite microspar and later, pore-filling ferroan calcite. The lack of concentric mineralogical patterns is another argument against concentric growth. Mozley (1996) as well as Raiswell and Fisher (2000) interpreted such patterns as evidence for pervasive growth, and it seems very probable that the Gams siderite concretions indeed grew in a pervasive fashion.

It is generally more difficult to constrain the growth mode of calcite concretions, since early to late stage cements have more frequently been recognized in siderite concretions (Raiswell and Fisher, 2000). For the Steinbrunn calcite concretions no textural or element geochemical trends from center to margin were recognized, also indicating pervasive growth. Further, the lack of systematic changes in carbonate content and of trends in stable isotope compositions argue in favor of pervasive growth. And finally, the formation of the septarian cracks in the Steinbrunn concretions required a concretion body, which had reached its final volume at the time of crack formation, but was still in a plastic state (cf. Hounslow, 1997; Pratt, 2001). To summarize, the growth mode of the Steinbrunn calcite concretions cannot be reconstructed with certainty, but pervasive growth seems more likely than concentric growth.

5.3 Formation of the Steinbrunn septaria

The calcite concretions of Steinbrunn contain abundant septarian cracks, which is a common phenomenon (Astin, 1986; Pratt, 2001). To date, various scenarios of septaria formation have been brought forward. Astin (1986) suggested that septarian cracks are the result of tensile stress caused by overpressure applied on the concretion and its host, Duck (1995) interpreted them as subaqueous shrinkage cracks generated by the conversion of a calcium "soap" of fatty acids to calcite, Sellés-Martínez (1996) suggested amplification of stress around a stiff concretion in a more plastic sediment, finally Hounslow (1997) suggested a scenario similar to that of Astin (1986) with the difference that he assumed higher pressure inside the concretion body than in the surrounding sediments. This higher pore pressure within the concretion body was suggested to be caused by permeability loss due to cementation of the concretion (Hounslow, 1997). The scenarios of Sellés-Martínez (1996) and Hounslow (1997) could well apply to the Steinbrunn calcite concretions, as they represent poorly permeable concretions enclosed in an unconsolidated sediment.

Other theories for crack formation are (1) chemical desiccation of a colloid, (2) gas expansion after gas production from the decay of organic matter, or (3) syneresis of a gel-like intermediate state of the interior (Sellés-Martínez, 1996; Pratt, 2001; Pearson et al., 2005). Pratt (2001) presented an innovative idea by linking crack formation to earthquake-induced ground motion, assuming concretions with stiff outer parts, while the concretion interiors were still soft. If septarian cracks show an orientation in horizontal sections, this may indicate anisotropic stress induced by tectonics or directional anisotropy in the growth rates (Astin 1986; Hounslow, 1997). Since the wider Steinbrunn region experienced tectonic deformation (Peres-

son and Decker, 1997; Exner et al., 2009), tectonic stress is also a feasible explanation for the formation of septarian cracks in the Steinbrunn concretions. However, also anisotropic growth seems possible, as the cracks are oriented parallel to the elongation in concretions, from which horizontal sections were taken (Figure 6C). Wieninger (2009) suggested a combination of the scenarios of Astin (1986), Hounslow (1997), and Pratt (2001) for the calcite concretions of Steinbrunn. Based on our observations the scenario of Astin (1986) seems less likely to account for crack formation in the Steinbrunn concretions, because it does not consider the problem of different stresses acting on the concretions and the less rigid host sediment. Unfortunately, the samples of the Steinbrunn concretions have not been taken orientated. Therefore, an unequivocal assessment of the putative role of tectonic stress in crack formation cannot be made.

5.4 Precipitation of carbonate cements – the effects of microbial remineralization of organic matter on concretion genesis

5.4.1 Biogeochemical processes involved in the formation of carbonate concretions

It is widely accepted that carbonate concretions may be products of microbial metabolism in the sedimentary column (e.g. Irwin et al., 1977; Loyd et al., 2012a). Below, it will be documented in brief how iron reduction, sulfate reduction, and methanogenesis can induce carbonate precipitation.

iron reduction

$$(CH_2O)_{106}(NH_3)_{16}H_3PO_4 + 424Fe(OH)_{3\,(s)} + 742CO_2 + 13.5H^+ \rightarrow 15NH_4^+ + 0.5HPO_4^{2-} + 0.5H_2PO_4 + 848HCO_3^- + 424Fe^{2+} + 318H_2O \quad (1)$$

sulfate reduction

$$(CH_2O)_{106}(NH_3)_{16}H_3PO_4 + 53SO_4^{2-} + 13.5H^+ \rightarrow {}^{\circledR} 15NH_{4+} + 0.5HPO_4^{2-} + 0.5H_2PO_{4-} + 53CO_2 + 53HCO_3^- + 53HS^- + 53H_2O \quad (2)$$

methanogenesis

$$2HCO_3^- + 4H_2 \rightarrow CH_4 + CO_3^{2-} + 3H_2O \quad (3)$$

Where applicable, reactions involving organic carbon are written in accordance with the Redfield Ratio (cf. Loyd et al., 2012a). Iron reduction (eq. 1) consumes a large quantity of protons and produces bicarbonate. Sulfate reduction (eq. 2) generates carbon dioxide and decreases therefore the pH, but it also generates bicarbonate, which rises carbonate alkalinity. Hydrogenotrophic methanogenesis (eq. 3) does not produce bicarbonate, but it increases the pH unlike acetoclastic methanogenesis. Because of this, the latter process is unlikely to trigger carbonate precipitation (but see Meister et al., 2011). Both factors, bicarbonate production and pH increase can contribute to the formation of carbonate minerals (eq. 4 from Coleman et al., 1985; eq. 5 modified after Coleman et al., 1985):

precipitation of calcite

$$Ca^{2+} + HCO_3^- + OH^- \rightarrow CaCO_3 + H_2O \quad (4)$$

precipitation of siderite

$$Fe^{2+} + HCO_3^- + OH^- \rightarrow FeCO_3 + H_2O \quad (5)$$

The acidity generated by sulfate reduction is commonly consumed by biogenic or abiogenic reduction of ferric iron in marine sediments. Ferric iron can be reduced abiogenically with the sulfide produced by bacterial sulfate reduction. Sulfide has a very high affinity to iron and if both are present in the system, iron monosulfides will precipitate, which may be subsequently transformed into pyrite (eq. 6 and 7 from Loyd et al. 2012a).

pyrite formation

$$5H^+ + 2Fe(OH)_{3\,(s)} + HS^- \rightarrow 2Fe^{2+} + S^\circ + 6H_2O \quad (6)$$

$$Fe^{2+} + HS^- + S^\circ_{(s)} \rightarrow FeS_{2\,(s)} + H^+ \quad (7)$$

Although the precipitation reaction (eq. 7) releases protons, this effect is compensated by the reduction of iron (eq. 1 and 6), which is necessary for pyrite formation. Carbonate precipitation through sulfate reduction is preferentially favored in the presence of sufficient iron, for which neo-formed pyrite is an indicator. The common framboidal habit of crystal aggregates of pyrite, as observed in the Steinbrunn concretions, is additional but not necessarily conclusive evidence for bacterial sulfate reduction (Coleman and Raiswell, 1995; Wilkin and Barnes, 1997; Ohfuji and Rickard, 2005). The presence of framboidal pyrite together with the characteristic markers for sulfate-reducing bacteria and low $\delta^{13}C$ values (see below) in the calcite concretions, thus, strongly point to an organic origin of the carbonate carbon.

If bacterial oxidation of organic matter or hydrogenotrophic methanogenesis were involved in the precipitation of carbonate, this is commonly reflected in the stable carbon isotopic composition of the resultant carbonate minerals (Irwin et al., 1977; Coleman et al., 1985; Siegel et al., 1987; Raiswell and Fisher, 2004). Iron- and sulfate-reducing bacteria most commonly assimilate carbon heterotrophically in marine sedimentary environments. The generated carbonate species are not fractionated significantly during the oxidation process and have consequently similar $\delta^{13}C$ values like the source from which they derived (Irwin et al., 1977). Marine organic matter has $\delta^{13}C$ values between -30‰ and -20‰ (Irwin et al., 1977; Siegel et al., 1987; Ziegenbalg et al., 2012). Nevertheless, the $\delta^{13}C$ values of the carbonate carbon are commonly higher than those of the parent organic matter, because marine dissolved inorganic carbon with its $\delta^{13}C$ value of around 0‰ is admixed during the precipitation process (Irwin et al., 1977; Coleman et al., 1985; Peckmann and Thiel, 2004). Consequently, the $\delta^{13}C$ values of diagenetic carbonate precipitated in the zones of iron reduction and sulfate reduction commonly fall between -30‰ and 0‰, depending on the mixing of the two or more carbon sources (Irwin et al., 1977; Coleman et al., 1985; 1993; Peckmann et al., 1999; Raiswell and Fisher, 2004; Loyd et al.,

2012a; 2012b). In contrast, hydrogenotrophic methanogenic archaea are highly selective in terms of their carbon source and preferentially take up $^{12}CO_2$, which results in a residual dissolved carbonate pool that is strongly enriched in ^{13}C ($\delta^{13}C$ values of +24‰; Boehme et al., 1996). Carbonate minerals precipitated in the zone of methanogenesis have therefore positive $\delta^{13}C$ values, again depending on the extent of mixing of different carbon sources (Irwin et al., 1977; Siegel et al., 1987; Kiriakoulakis et al., 2000; Lash and Blood, 2004; Raiswell and Fisher, 2004; Pearson and Nelson, 2005; Ziegenbalg et al., 2010; Hoffmann-Sell et al., 2011; Meister et al., 2011; Kuechler et al., 2012; Natalicchio et al., 2012; Birgel et al., 2015).

The oxygen stable isotope composition of carbonate minerals is a function of the parent fluid composition and the temperature during precipitation; if one of these parameters is known, the second can be calculated (Irwin et al., 1977; Loyd et al., 2014). But also the biological fractionation of oxygen isotopes needs to be taken into consideration (e.g. Kiriakoulakis et al., 2000; Raiswell and Fisher, 2000). Mortimer and Coleman (1997) reported that iron-reducing bacteria preferentially take up ^{16}O, which induces the precipitation of ^{18}O depleted siderite. Antler et al. (2013) compared the enrichment in ^{18}O and ^{34}S of the residual sulfate pool during sulfate reduction. They further looked into the effects of variable organic matter contents and sulfate reduction rates. If a lot of organic matter was available and sulfate reduction rates were high, the $\delta^{18}O$ values of the residual sulfate were found to increase more slowly in relation to the $\delta^{34}S$ values. Indeed, the biological effects of iron reduction and sulfate reduction are unexpectedly high and in the same range of other factors lowering the $\delta^{18}O$ values of diagenetic carbonates, such as temperature, influx of meteoric water, or precipitation of other, ^{18}O-rich minerals (Pye et al., 1990; Mozley and Wersin, 1992; Mortimer and Coleman, 1997; Raiswell and Fisher, 2000; Pearson and Nelson, 2005; Loyd et al., 2014). Overall the $\delta^{18}O$ values of the Steinbrunn calcite concretions (mean: -8.4‰) and the host sediment (-6.0‰) could reflect either the effect of microbial fractionation, a mixing with meteoric waters, recrystallization at higher temperatures, or a combination of all mechanisms. Interestingly, the observed positive correlation of the highest and lowest $\delta^{13}C$ and $\delta^{18}O$ values, respectively, found for the Steinbrunn concretions agrees with fractionation caused by sulfate reduction. Among the factors listed above only recrystallization at higher temperatures seems unlikely, whereas the relative significance of the other factors cannot be conclusively evaluated with the present data set.

5.4.2 Evidence for a bacterial influence on concretion formation

5.4.2.1 Gams siderite concretions

Based on the low $\delta^{13}C$ values of the Gams concretions alone (as low as −11.1‰), it is feasible that siderite precipitation took place either in the iron reduction zone or the sulfate reduction zone. However, since siderite precipitated, the sulfate reduction zone can be excluded, because ferrous iron has a higher affinity to sulfide ions than to carbonate ions (e.g. Coleman et al., 1985). As long as sulfide is present it will outcompete carbonate in its affinity to iron. Only if all sulfide is used up and iron is still available, the precipitating carbonates can be ferroan calcite, ferroan dolomite, ankerite, or siderite (Coleman et al., 1985; Pye et al., 1990; Coleman et al., 1993; Coleman and Raiswell, 1995; Duan et al., 1996; Mortimer et al., 2011). In most natural systems, not enough reactive iron is available and the most common assemblage is iron-free calcite with pyrite (Coleman et al., 1985; Coleman and Raiswell, 1995). Hence, the precipitation of siderite concretions requires a system with very low sulfate concentrations or, alternatively, high concentrations of reactive iron. This is the reason why many diagenetic siderites were thought to have formed in freshwater environments by methanogenesis (Coleman et al., 1993). However, this option can be excluded for the Gams siderite concretions for several reasons. First, methanogenesis would have produced a characteristic, positive $\delta^{13}C$ signature, which is not present in the Gams concretions. Second, the siderite concretions are clearly of a marine origin, as revealed by the deep marine depositional setting with turbidites (Wagreich et al., 2011). And indeed, the $\delta^{13}C$ values (mean: -9.2‰) and $\delta^{13}O$ values (mean: +0.5‰) are typical for marine siderite (cf. Mozley and Wersin, 1992). Alternatively, the siderite of the Gams concretions can have precipitated in a sulfide-free zone of iron reduction above the zone of sulfate reduction with sulfide present (cf. Coleman et al., 1985; Pye et al., 1990; Coleman et al., 1993; Duan et al., 1996). In case of marine systems with extraordinarily high input of ferric iron and reworking of surface deposits, diagenetic iron sulfides are exposed to a great degree to reoxidation (e.g., Konhauser, 2007). Organic matter becomes progressively consumed, while there is still recycled ferric iron available. Thus, iron reduction exceeds sulfate reduction, which enables the precipitation of ferrous iron carbonates. Mortimer et al. (2011) suggested a scenario where coupled biotic and abiotic iron reduction produces elemental sulfur and siderite in a recent salt marsh (north Norfolk coast, UK). In their scenario, high sedimentation rates preserved reactive ferric iron in depth, while seawater sulfate became relatively diluted to the point that iron reduction exceeded sulfate reduction at the site of concretion formation. The authors stressed that reactive iron contents are typically higher in salt marshes than in other marine sediments. Interestingly, the host sediments of the Gams concretions reflect very high sedimentation rates (Wagreich et al., 2011), which could have favored iron reduction due to high input of iron-rich detritus, dilution of sulfate, and subsequent precipitation of siderite. The prerequisite for this scenario is that the rates of sulfate reduction were low enough, maybe due to recycling of iron sulfides, to prevent the diffusion of hydrogen sulfide to the site of iron reduction, which would have led to the dissolution of siderite and subsequent pyrite formation (cf. Coleman et al., 1985, Konhauser, 2007).

The mean $\delta^{13}C$ value of the siderite concretions (-9.2‰) is more negative than that of the Steinbrunn calcite concretions.

Therefore, a slightly higher contribution of organic matter derived carbon or a more ^{13}C depleted organic matter source can be assumed. The long-term fluctuations of $\delta^{13}C$ values of marine carbonate and organic matter are negligible for the comparison of the Eocene siderite concretions and the Miocene calcite concretions (cf. Hayes et al., 1999). The dispersed carbonate of the Gams host rocks shows mostly marine $\delta^{13}C$ values and lower $\delta^{18}O$ values than the concretion bodies. It seems therefore likely that ^{18}O depleted, possibly warm and/or meteoric waters circulated more easily through the host sediment than through the less permeable concretions. The marine $\delta^{13}C$ values of the carbonate in the host rocks in comparison with the negative $\delta^{13}C$ values of the concretions confirm that organic matter remineralization was most pronounced at the sites of concretion growth.

Unfortunately, iron-reducing bacteria are not known to produce lipids that would be specific for this group of Bacteria and are stable on geological time scales at the same time (Coleman et al., 1993; Eickhoff et al., 2013), which could have helped confirming this scenario. Moreover, the high thermal overprint at the Gams locality erased pristine lipid signatures. The biomarker patterns of the siderite concretion are sparse, unspecific and especially the lipid fraction after decalcification – which is diagnostic for benthic microorganisms involved in mineral formation – is almost barren of lipids. For example, sample GA-4 lacks hopanoic acids, hopanes disappear after decalcification, and branched fatty acids are less abundant after decalcification. As a consequence, it must be concluded that these molecular fossils are not intrinsic to the depositional or diagenetic environment but represent later stage allochthonous input. The only signatures, which seem to be primary, are long-chain *n*-alkanes and very unspecific *n*-fatty acids. The relative content of marine organic material is overall higher compared to the Steinbrunn calcite concretions (TARs and LMW/HMW ratios, Tables 3 and 5), which is in accord with the geological setting.

5.4.2.2 Steinbrunn calcite concretions

The average $\delta^{13}C$ values of -5.8‰ of the Steinbrunn concretions point to a mixture of carbonate derived from the oxidation of organic carbon by iron reduction or sulfate reduction with dissolved inorganic carbon (cf. Irwin et al., 1977; Peckmann and Thiel, 2004). In contrast to the Gams siderite concretions, the Steinbrunn calcite concretions contain lipid biomarkers that are of high specificity for Bacteria. Short-chain branched fatty acids derive from various bacterial sources (Table 6), and are more persistent than unsaturated fatty acids. Among the most specific branched fatty acids is 10Me-$C_{16:0}$ fatty acid, which occurs in traces in the calcite concretions. This compound is particularly abundant in the sulfate-reducing bacterial genus *Desulfobacter* (e.g. Coleman et al., 1993). Interestingly, the overall minor amounts of *iso*-$C_{15:0}$ and *anteiso*-$C_{15:0}$, *iso*-$C_{16:0}$ as well as *iso*-$C_{17:0}$ and *anteiso*-$C_{17:0}$ increase in the extracts after decalcification. Moreover, the predominance of *anteiso*- over *iso*-fatty acids in the Steinbrunn concretions is in accord with findings of Rütters et al. (2001), who analyzed cultures of the sulfate reducer *Desulfosarcina variabilis*. Birgel et al. (2011) recognized a similar pattern in lipids extracted from methane-seep carbonates from an environment populated by *Desulfosarcina/Desulfococcus* species. It seems likely that *Desulfosarcina* or other sulfate-reducing bacteria have been the producers of the *iso*- and *anteiso*-fatty acids preserved in the Steinbrunn concretions.

Apart from aliphatic compounds, hopanoids – biomarkers of Bacteria – are present in appreciable amounts. Although many bacteria have the theoretical ability to synthesize hopanoids, only about 10% of them effectively do this (Rohmer et al., 1984; Pearson et al., 2007). Hopanoids have traditionally been assumed to be restricted to aerobic bacteria. However, it was later shown that also strictly anaerobic bacteria can produce hopanoids (Sinninghe Damsté et al., 2004; Fischer et al., 2005; Härtner et al., 2005; Blumenberg et al., 2006; Eickhoff et al., 2013). Among other hopanoids, diploptene (hop-22(29)-ene) was detected in pure cultures of sulfate-reducing bacteria of the genus *Desulfovibrio* and iron-reducing bacteria of the genus *Geobacter* (Härtner et al., 2005; Blumenberg et al., 2006; Eickhoff et al., 2013). Diploptene was not the most abundant hopanoid in any of these studies, but it is interesting to note that its geological degradation product hop-17(21)-ene was found in the hydrocarbon extract after decalcification of the Steinbrunn concretions, and, hence, represents a pristine compound, possibly deriving from sulfate-reducing bacteria among other potential sources.

Trisnorhopanes (C_{27}) and norhopanes (C_{29}) are the most abundant hopanoids in the hydrocarbon fractions of the calcite concretions. However, as these compounds lost up to three carbon atoms from the C_{30} basic hopanoid backbone (cf. Farrimond et al., 2002; Talbot and Farrimond, 2007), they have lost any specificity. Similarly, ββ C_{32} hopanoic acid, the dominant hopanoid in the fatty acid fraction, cannot be assigned to a specific precursor. The circumstance that the primary, biological isomer (ββ) is more abundant than the secondary, geological isomer (αβ) reveals that organic matter preserved in the Steinbrunn concretions is of low maturity (cf. Farrimond et al., 2002). Apart from the greater abundance of αβ isomers among the hopanoids of the hydrocarbon fraction compared to the hopanoic acids, the shift of the hopanoic acids toward higher carbon numbers relative to the hopanes indicates that these groups of compounds derive from different sources. While hopanes span from C_{27} to C_{31}, hopanoic acids range from C_{30} to C_{34}. Likewise, the carbon number distribution patterns accompanied by the different isomerization patterns indicate that hopanes and hopanoic acids have different origins (cf. Farrimond et al., 2002). Hopanes with the notable exception of hop-17(21)-ene seem to be considerably older and probably have a terrestrial origin similar to the long-chain *n*-alkanes, whereas hopanoic acids more likely derived from water column or unspecified benthic bacteria.

To sum up, the occurrence of framboidal pyrite, short-chain, branched fatty acids, and hop-17(21)-ene, as well as the low

$\delta^{13}C_{calcite}$ values are best explained by the former presence of sulfate-reducing bacteria and their impact on the formation of calcite concretions. Although the environment was not fully marine any more, the pore water still contained sufficient sulfate to enable further oxidation of organic matter by bacterial sulfate reduction.

6. Conclusions

For a better comprehensibility of the different aspects covered in the discussion, a graphic scheme comparing the informative value of data gained from the Gams and Steinbrunn concretions is given in Figure 17.

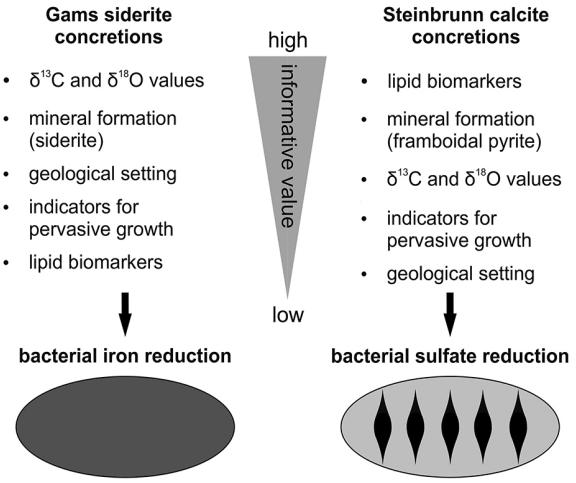

Figure 17: Graphic scheme comparing the informative value of data gained from the Gams and Steinbrunn concretions.

6.1 Siderite concretions

The Gams siderite concretions formed approximately 55 Ma ago at shallow sediment depth within sediments deposited in a deep water environment. The geological setting with high sedimentation rates and the deposition of turbidites account for high input of detrital iron-bearing minerals, which is believed to have favored ferric iron reduction over bacterial sulfate reduction. Several observations agree with the scenario that siderite formation was driven by microbial iron reduction.

- The $\delta^{13}C$ values of the concretions are typical for carbonate resulting from the oxidation of organic matter, which is even more significant since the host rocks reveal values typical for marine carbonate. Sulfate reduction can be excluded as driving force of siderite precipitation, since its product sulfide has a higher affinity to ferrous iron than carbonate ions, preventing precipitation of iron carbonate minerals.
- The difference of $\delta^{18}O$ values between carbonate dispersed in the host rocks and the concretions indicates that early cementation of the concretion preserved a marine signal, while the still permeable host sediments were affected by a later stage overprint by ^{18}O-depleted waters.
- The Gams siderite concretions grew in a pervasive mode, since no petrographic, mineralogical, element, or stable isotope trends have been recognized from the center to the margin of the concretions.

6.2 Calcite concretions

The septarian calcite concretions of Steinbrunn formed ca. 10 Ma ago. Although the geological setting had been characterized as a brackish to limnic pond, the pore waters apparently contained sufficient sulfate to allow for extensive bacterial sulfate reduction.

- Abundant corallinaceans, enclosed in the host rock and cemented by concretions, reflect the input of detritus from the Badenian marine Leithakalk from the nearby elevated area of the Leithagebirge.
- Significant terrestrial input is confirmed by abundant long-chain *n*-alkanes, which derive from plant waxes.
- The depletion of ^{18}O in the calcite of the concretions and their host sediment indicate the influx of meteoric waters or fractionation in the course of bacterial sulfate reduction, whereas high temperature overprinting seems unlikely.
- Low $\delta^{13}C_{calcite}$ values confirm that the carbonate is partly derived from the oxidation of organic matter. The ^{13}C depletion, the presence of framboidal pyrite, hop-17(21)-ene, a degradation product of diploptene, and short-chain, branched fatty acids indicate that sulfate-reducing bacteria favored concretion growth.
- The circumstance that no element or isotope trends from the center to the margin of the concretions have been observed accounts for pervasive growth rather than concentric growth.
- The preferred parallel orientation of the septarian cracks in horizontal sections may have resulted from anisotropic, lateral stress, which is in accord with the tectonic history of the Steinbrunn locality. Likewise, cracking could have been triggered by seismic shocks caused by earthquakes or by an excess pore pressure within the concretions caused by the loss of permeability due to cementation.

This work exemplifies that concretions represent an excellent window into the geomicrobiology of ancient sediments. Future work aiming at the optimization of the use of this archive should use new cutting-edge approaches such as the high resolution analysis of carbonate-associated sulfur isotopes and phase-specific element and isotope analyses, applying techniques like LA-ICP-MS, MicroSIMS, and NanoSIMS. There is still a lot of potential for future research in these fascinating products of past microbial activity.

7. Acknowledgments

We thank Beatrix Bethke (Vienna) for technical support during biomarker analysis, Susanne Gier (Vienna) for X-ray diffraction analysis, Patrick Meister (Vienna) for discussion on microbially-mediated carbonate formation, Sylvain Richoz (Graz) for the analysis of the carbon and oxygen stable isotope

composition of carbonate samples, Erik Wolfgring (Vienna) for help with the identification of foraminifers, and Leopold Slawek (Vienna) for thin section preparation. Comments by Luca Martire (Turin) and an anonymous referee helped improve the manuscript. Lydia Baumann acknowledges financial support of her academic studies by the Studienbeihilfenbehörde, Stipendienstelle Wien, Bundesministerium für Wissenschaft, Forschung und Wirtschaft, Austria.

8. References

Antler, G., Turchyn, A.V., Rennie, V., Herut, B. and Sivan, O., 2013. Coupled sulfur and oxygen isotope insight into bacterial sulfate reduction in the natural environment. Geochimica et Cosmochimica Acta, 118, 98-117. http://dx.doi.org/10.1016/j.gca.2013.05.005

Arning, E.T., Birgel, D., Brunner, B. and Peckmann, J., 2009. Bacterial formation of phosphatic laminites off Peru. Geobiology, 7, 295-307. http://dx.doi.org/10.1111/j.1472-4669.2009.00197.x

Astin, T.R., 1986. Septarian crack formation in carbonate concretions from shales and mudstones. Clay Minerals, 21, 617-631. http://www.minersoc.org/pages/Archive-CM/Volume_21/21-4-617.pdf

Birgel, D., Thiel, V., Hinrichs, K.-U., Elvert, M., Campbell, K.A., Reitner, J., Farmer J.D. and Peckmann, J., 2006. Lipid biomarker patterns of methane-seep microbialites from the Mesozoic convergent margin of California. Organic Geochemistry, 37, 1289-1302. http://dx.doi.org/10.1016/j.orggeochem.2006.02.004

Birgel, D., Feng, D., Roberts, H.H. and Peckmann, J., 2011. Changing redox conditions at cold seeps as revealed by authigenic carbonates from Alaminos Canyon, northern Gulf of Mexico. Chemical Geology, 285, 82-96. http://dx.doi.org/10.1016/j.chemgeo.2011.03.004

Birgel, D., Meister, P., Lundberg, R., Horath, T.D., Bontognali, T.R.R., Bahniuk, A.M., De Rezende, C.E., Vasconcelos, C. and McKenzie, J.A., 2015. Methanogenesis produces strong ^{13}C enrichment in stromatolites of Lagoa Salgada, Brazil: a modern analogue for Palaeo-/Neoproterozoic stromatolites? Geobiology, 13, 245-266. http://dx.doi.org/10.1111/gbi.12130

Bligh, E.G. and Dyer, W.J., 1959. A rapid method of total lipid extractions and purification. Canadian Journal of Biochemistry and Physiology, 37, 911-917. http://dx.doi.org/10.1139/o59-099

Blome, C.D. and Albert, N.R., 1985. Carbonate concretions: An ideal sedimentary host for microfossils. Geology, 13, 212-215. http://dx.doi.org/10.1130/0091-7613(1985)13<212:CCAISH>2.0.CO;2

Blumenberg, M., Krüger, M., Nauhaus, K., Talbot, H.M., Oppermann, B.I., Seifert, R., Pape, T. and Michaelis, W., 2006. Biosynthesis of hopanoids by sulfate-reducing bacteria (genus *Desulfovibrio*). Environmental Microbiology, 8, 1220-1227. http://dx.doi.org/10.1111/j.1462-2920.2006.01014.x

Boehme, S.E., Blair, N.E., Chanton, J.P. and Martens, C.S., 1996. A mass balance of ^{13}C and ^{12}C in an organic-rich methane-producing marine sediment. Geochimica et Cosmochimica Acta, 60, 3835-3848. http://dx.doi.org/10.1016/0016-7037(96)00204-9

Bourbonniere, R.A. and Meyers, P.A., 1996. Sedimentary geolipid records of historical changes in the watersheds and productivities of Lakes Ontario and Erie. Limnology and Oceanography, 41, 352-359. http://dx.doi.org/10.4319/lo.1996.41.2.0352

Brocks, J.J., Love, G.D., Summons, R.E., Knoll, A.H., Logan, G.A. and Bowden S.A., 2005. Biomarker evidence for green and purple sulphur bacteria in a stratified Palaeoproterozoic sea. Nature, 437, 866-870. http://dx.doi.org/10.1038/nature04068

Coleman, M.L., Berner, R.A., Durand, B., Meadows, P.S. and Eglinton, G., 1985. Geochemistry of diagenetic non-silicate minerals: kinetic considerations. Philosophical Transactions of the Royal Society of London A, 315, 39-56. http://dx.doi.org/10.1098/rsta.1985.0028

Coleman, M.L., Hedrick, D.B., Lovley, D.R., White, D.C. and Pye, K., 1993. Reduction of Fe(III) in sediments by sulphate-reducing bacteria. Nature, 361, 436-438. http://dx.doi.org/10.1038/361436a0

Coleman, M.L. and Raiswell, R., 1995. Source of carbonate and origin of zonation in pyritiferous carbonate concretions: evaluation of a dynamic model. American Journal of Science, 295, 282-308. http://dx.doi.org/10.2475/ajs.295.3.282

Dickson, J.A.D., 1965. A modified staining technique for carbonates in thin section. Nature, 205, 587-587. http://dx.doi.org/10.1038/205587a0

Duan, W.M., Hedrick, D.B., Pye, K., Coleman, M.L. and White, D.C., 1996. A preliminary study of the geochemical and microbiological characteristics of modern sedimentary concretions. Limnology and Oceanography, 41, 1404-1414. http://dx.doi.org/10.4319/lo.1996.41.7.1404

Duck, R.W., 1995. Subaqueous shrinkage cracks and early sediment fabrics preserved in Pleistocene calcareous concretions. Journal of the Geological Society, London, 152, 151-156. http://dx.doi.org/10.1144/gsjgs.152.1.0151

Egger, H., Rögl, F. and Wagreich, M., 2004. Biostratigraphy and facies of Paleogene deep-water deposits at Gams (Gosau Group, Austria). Annalen des Naturhistorischen Museums Wien, 106A, 281-307. http://www.nhm-wien.ac.at/jart/prj3/nhm/data/uploads/mitarbeiter_dokumente/roegl/2004_Egger_et_al_Gams.pdf

Eglinton, G., Gonzalez, A.G., Hamilton, R.J. and Raphael, R.A., 1962. Hydrocarbon constituents of the wax coatings of plant leaves: a taxonomic survey. Phytochemistry, 1, 89-102. http://dx.doi.org/10.1016/S0031-9422%2800%2988006-1

Eglinton, G. and Hamilton, R.J., 1967. Leaf epicuticular waxes. Science, 156, 1322-1335. http://dx.doi.org/10.1126/science.156.3780.1322

Eickhoff, M., Birgel, D., Talbot, H.M., Peckmann, J. and Kap-

pler, A., 2013. Bacteriohopanoid inventory of *Geobacter sulfurreducens* and *Geobacter metallireducens*. Organic Geochemistry, 58, 107-114. http://dx.doi.org/10.1016/j.orggeochem.2013.02.013

El-Shafeiy, M., Birgel, D., El-Kammar, A., El-Barkooky, A., Wagreich, M., Mohamed, O. and Peckmann, J., 2014. Palaeoecological and post-depositional changes recorded in Campanian-Maastrichtian black shales, Abu Tartur plateau, Egypt. Cretaceous Research, 50, 38-51. http://dx.doi.org/10.1016/j.cretres.2014.03.022

Exner, U., Draganits, E. and Grasemann, B., 2009. Folding in Miocene, unconsolidated clastic sediments (Vienna basin, Austria) – gravitational versus tectonic forces. Trabajos de Geología, Universidad de Oviedo, 29, 269-272. http://www.researchgate.net/publication/264361562_Folding_in_Miocene_unconsolidated_clastic_sediments_%28Vienna_basin_Austria%29__gravitational_versus_tectonic_forces

Farrimond, P., Griffiths, T. and Evdokiadis, E., 2002. Hopanoic acids in Mesozoic sedimentary rocks: their origin and relationship with hopanes. Organic Geochemistry, 33, 965-977. http://dx.doi.org/10.1016/S0146-6380%2802%2900059-1

Faupl, P. and Wagreich, M., 1996. Basin analysis of the Gosau Group of the Northern Calcareous Alps (Turonian-Eocene, Eastern Alps). In G. Wessely and W. Liebl (eds.), Oil and Gas in Alpidic Thrustbelts and Basins of Central and Eastern Europe. EAGE Special Publication, 5, 127-135. http://dx.doi.org/10.3997/2214-4609.201410235

Fischer, W.W., Summons, R.E. and Pearson, A., 2005. Targeted genomic detection of biosynthetic pathways: anaerobic production of hopanoid biomarkers by a common sedimentary microbe. Geobiology, 3, 33-40. http://dx.doi.org/10.1111/j.1472-4669.2005.00041.x

Grundtner, M.-L., 2009. Sedimentologisches Profil der Sandgrube Steinbrunn/Bgld. Bachelor's thesis, Universität Wien, Vienna, Austria, 54 pp.

Grundtner, M.-L., Harzhauser, M., Mandic, O., Draganits, E., Gier, S., Exner, U. and Wagreich, M., 2009. Zur Sedimentologie der Sandgrube Steinbrunn (Pannonium, Österreich). Jahrbuch der Geologischen Bundesanstalt, 149, 441-451. http://www.nhm-wien.ac.at/jart/prj3/nhm/data/uploads/mitarbeiter_dokumente/harzhauser/2009/2009_Grundtner_et_al.pdf

Guido, A., Heindel, K., Birgel, D., Rosso, A., Mastandrea, A., Sanfilippo, R., Russo, F. and Peckmann, J., 2013. Pendant bioconstructions cemented by microbial carbonate in submerged marine caves (Holocene, SE Sicily). Palaeogeography, Palaeoclimatology, Palaeoecology, 388, 166-180. http://dx.doi.org/10.1016/j.palaeo.2013.08.007

Härtner, T., Straub, K.L. and Kannenberg, E., 2005. Occurrence of hopanoid lipids in anaerobic *Geobacter* species. FEMS Microbiology Letters, 243, 59-64. http://dx.doi.org/10.1016/j.femsle.2004.11.039

Hayes, J.M., Strauss, H. and Kaufman, A.J., 1999. The abundance of ^{13}C in marine organic matter and isotopic fractionation in the global biogeochemical cycle of carbon during the past 800 Ma. Chemical Geology, 161, 103-125. http://dx.doi.org/10.1016/S0009-2541(99)00083-2

Heindel, K., Richoz, S., Birgel, D., Brandner, R., Klügel, A., Krystyn, L., Baud, A., Horacek, M., Mohtat, T. and Peckmann, J., 2015. Biogeochemical formation of calyx-shaped carbonate crystal fans in the subsurface of the Early Triassic seafloor. Gondwana Research, 27, 840-861. http://dx.doi.org/10.1016/j.gr.2013.11.004

Hoffmann-Sell, L., Birgel, D., Arning, E.T., Föllmi, K.B. and Peckmann, J., 2011. Archaeal lipids in Neogene dolomites (Monterey and Sisquoc Formations, California) – Planktic versus benthic archaeal sources. Organic Geochemistry, 42, 593-604. http://dx.doi.org/10.1016/j.orggeochem.2011.04.008

Hounslow, M.W., 1997. Significance of localized pore pressures to the genesis of septarian concretions. Sedimentology, 44, 1133-1147. http://dx.doi.org/10.1046/j.1365-3091.1997.d01-64.x

Irwin, H., Curtis, C. and Coleman, M., 1977. Isotopic evidence for source of diagenetic carbonates formed during burial of organic-rich sediments. Nature, 269, 209-213. http://dx.doi.org/10.1038/269209a0

Kiriakoulakis, K., Marshall, J.D. and Wolff, G.A., 2000. Biomarkers in a Lower Jurassic concretion from Dorset (UK). Journal of the Geological Society, London, 157, 207-220. http://dx.doi.org/10.1144/jgs.157.1.207

Konhauser, K., 2007. Introduction to Geomicrobiology. Blackwell Science Ltd, 425 pp.

Kuechler, R.R., Birgel, D., Kiel, S., Freiwald, A., Goedert, J.L., Thiel, V. and Peckmann, J., 2012. Miocene methane-derived carbonates from southwestern Washington, USA and a model for silicification at seeps. Lethaia, 45, 259-273. http://dx.doi.org/10.111/j.1502-3931.2011.00280.x

Lash, G.G. and Blood, D., 2004. Geochemical and textural evidence for early (shallow) diagenetic growth of stratigraphically confined carbonate concretions, Upper Devonian Rhinestreet black shale, western New York. Chemical Geology, 206, 407-424. http://dx.doi.org/10.1016/j.chemgeo.2003.12.017

Loeblich, A.R. and Tappan, H.N, 1987. Foraminiferal genera and their classification. Van Nostrand Reinhold, New York, 1694 pp.

Loyd, S.J., Berelson, W.M., Lyons, T.W., Hammond, D.E. and Corsetti, F.A., 2012a. Constraining pathways of microbial mediation for carbonate concretions of the Miocene Monterey Formation using carbonate-associated sulfate. Geochimica et Cosmochimica Acta, 78, 77-98. http://dx.doi.org/10.1016/j.gca.2011.11.028

Loyd, S.J., Corsetti, F.A., Eiler, J.M. and Tripati, A.K., 2012b. Determining the diagenetic conditions of concretion formation: assessing temperatures and pore waters using clumped isotopes. Journal of Sedimentary Research, 82, 1006-1016. http://dx.doi.org/10.2110/jsr.2012.85

Loyd, S.J., Dickson, J.A.D., Boles, J.R. and Tripati, A.K., 2014. Clumped-isotope constraints on cement paragenesis in septarian concretions. Journal of Sedimentary Research, 84, 1170-1184. http://dx.doi.org/10.2110/jsr.2014.91

Meister, P., Gutjahr, M., Frank, M., Bernasconi, S.M., Vasconce-

los, C. and McKenzie, J.A., 2011. Dolomite formation within the methanogenic zone induced by tectonically driven fluids in the Peru accretionary prism. Geology, 39, 563-566. http://dx.doi.org/10.1130/G31810.1

Mortimer, R.J.G. and Coleman, M.L., 1997. Microbial influence on the oxygen isotopic composition of diagenetic siderite. Geochimica et Cosmochimica Acta, 61, 1705-1711. http://dx.doi.org/10.1016/S0016-7037(97)00027-6

Mortimer, R.J.G., Galsworthy, A.M.J., Bottrell, S.H., Wilmot, L.E. and Newton, R.J., 2011. Experimental evidence for rapid biotic and abiotic reduction of Fe(III) at low temperatures in salt marsh sediments: a possible mechanism for formation of modern sedimentary siderite concretions. Sedimentology, 58, 1514-1529. http://dx.doi.org/10.1111/j.1365-3091.2011.01224.x

Mozley, P.S. and Wersin, P., 1992. Isotopic composition of siderite as an indicator of depositional environment. Geology, 20, 817-820. http://dx.doi.org/10.1130/0091-7613(1992)020<0817:ICOSAA>2.3.CO;2

Mozley, P.S., 1996. The internal structure of carbonate concretions in mudrocks: a critical evaluation of the conventional concentric model of concretion growth. Sedimentary Geology, 103, 85-91. http://dx.doi.org/10.1016/0037-0738(95)00087-9

Müller, G. and Gastner, M., 1971. The "Karbonat-Bombe", a simple device for the determination of the carbonate content in sediments, soils and other materials. Neues Jahrbuch für Mineralogie – Monatshefte, 10, 466-469. http://epic.awi.de/27239/1/Mll1971a.pdf

Natalicchio, M., Birgel, D., Dela Pierre, F., Martire, L., Clari, P., Spötl, C. and Peckmann, J., 2012. Polyphasic carbonate precipitation in the shallow subsurface: Insights from microbially-formed authigenic carbonate beds in upper Miocene sediments of the Tertiary Piedmont Basin (NW Italy). Palaeogeography, Palaeoclimatology, Palaeoecology, 329-330, 158-172. http://dx.doi.org/10.1016/j.palaeo.2012.02.026

Ohfuji, H. and Rickard, D., 2005. Experimental syntheses of framboids – a review. Earth-Science Reviews, 71, 147-170. http://dx.doi.org/10.1016/j.earscirev.2005.02.001

Pearson, M.J., Hendry, J.P., Taylor, C.W. and Russell, M.A., 2005. Fatty acids in sparry calcite fracture fills and microsparite cement of septarian diagenetic concretions. Geochimica et Cosmochimica Acta, 69, 1773-1786. http://dx.doi.org/10.1016/j.gca.2004.09.024

Pearson, M.J. and Nelson, C.S., 2005. Organic geochemistry and stable isotope composition of New Zealand carbonate concretions and calcite fracture fills. New Zealand Journal of Geology and Geophysics, 48, 395-414. http://dx.doi.org/10.1080/00288306.2005.9515122

Pearson, A., Flood Page, S.R., Jorgenson, T.L., Fischer, W.W. and Higgins, M.B., 2007. Novel hopanoid cyclases from the environment. Environmental Microbiology, 9, 2175-2188. http://dx.doi.org/10.1111/j.1462-2920.2007.01331.x

Peckmann, J., Paul, J. and Thiel, V., 1999. Bacterially mediated formation of diagenetic aragonite and native sulfur in Zechstein carbonates (Upper Permian, Central Germany). Sedimentary Geology, 126, 205-222. http://dx.doi.org/10.1016/S0037-0738(99)00041-X

Peckmann, J. and Thiel, V., 2004. Carbon cycling at ancient methane-seeps. Chemical Geology, 205, 443-467. http://dx.doi.org/10.1016/j.chemgeo.2003.12.025

Peresson, H. and Decker, K., 1997. Far-field effects of Late Miocene subduction in the Eastern Carpathians: E-W compression and inversion of structures in the Alpine-Carpathian-Pannonian region. Tectonics, 16, 38-56. http://dx.doi.org/10.1029/96TC02730

Peters, K.E., Walters, C.C. and Moldowan, J.M., 2005. The Biomarker Guide, Volume 2, Biomarkers and Isotopes in Petroleum Exploration and Earth History, 2nd ed.. Cambridge University Press, UK, 1157 pp.

Piller, W.E., Decker, K. and Haas, M., 1996. Exkursion A1: Sedimentologie und Beckendynamik des Wiener Beckens. Exkursionsführer SEDIMENT '96, 11. Sedimentologentreffen, Wien. – Berichte Geol. B.-A., 33, 41. http://www.landesmuseum.at/pdf_frei_remote/BerichteGeolBundesanstalt_33_0001-0041.pdf

Pratt, B.R., 2001. Septarian concretions: internal cracking caused by synsedimentary earthquakes. Sedimentology, 48, 189-213. http://dx.doi.org/10.1046/j.1365-3091.2001.00366.x

Pye, K., Dickson, J.A.D., Schiavon, N., Coleman, M.L. and Cox, M., 1990. Formation of siderite-Mg-calcite-iron sulphide concretions in intertidal marsh and sandflat sediments, north Norfolk, England. Sedimentology, 37, 325-343. http://dx.doi.org/10.1111/j.1365-3091.1990.tb00962.x

Raiswell, R. and Fisher, Q.J., 2000. Mudrock-hosted carbonate concretions: a review of growth mechanisms and their influence on chemical and isotopic compostition. Journal of the Geological Society, London, 157, 239-251. http://dx.doi.org/10.1144/jgs.157.1.239

Raiswell, R. and Fisher, Q.J., 2004. Rates of carbonate cementation associated with sulphate reduction in DSDP/ODP sediments: implications for the formation of concretions. Chemical Geology, 211, 71-85. http://dx.doi.org/10.1016/j.chemgeo.2004.06.020

Reitner, J., Peckmann, J., Blumenberg, M., Michaelis, W., Reimer A. and Thiel, V., 2005. Concretionary methane-seep carbonates and associated microbial communities in Black Sea sediments. Palaeogeography, Palaeoclimatology, Palaeoecology, 227, 18-30. http://dx.doi.org/10.1016/j.palaeo.2005.04.033

Rohmer, M., Bouvier-Nave, P. and Ourisson, G., 1984. Distribution of hopanoid triterpenes in prokaryotes. Journal of General Microbiology, 130, 1137-1150. http://dx.doi.org/10.1099/00221287-130-5-1137

Rommerskirchen, F., Plader, A., Eglinton, G., Chikaraishi, Y. and Rullkötter, J., 2006. Chemotaxonomic significance of distribution and stable carbon isotopic composition of long-chain alkanes and alkan-1-ols in C4 grass waxes. Organic Geochemistry, 37, 1303-1332. http://dx.doi.org/10.1016/j.orggeochem.2005.12.013

Rontani, J.-F. and Bonin, P., 2011. Production of pristane and phytane in the marine environment: role of prokaryotes.

Research in Microbiology, 162, 923-933. http://dx.doi.org/10.1016/j.resmic.2011.01.012

Rupp, C., 1986. Paläoökologie der Foraminiferen in der Sandschalerzone (Badenien, Miozän) des Wiener Beckens. Beiträge zur Paläontologie von Österreich, 12, 1-180.

Rütters, H., Sass, H., Cypionka, H. and Rullkötter, J., 2001. Monoalkylether phospholipids in the sulfate-reducing bacteria *Desulfosarcina variabilis* and *Desulforhabdus amnigenus*. Archives of Microbiology, 176, 435-442. http://dx.doi.org/10.1007/s002030100343

Sellés-Martínez, J., 1996. Concretion morphology, classification and genesis. Earth-Science Reviews, 41, 177-210. http://dx.doi.org/10.1016/S0012-8252(96)00022-0

Siegel, D.I, Chamberlain, S.C. and Dossert, W.P., 1987. The isotopic and chemical evolution of mineralization in septarian concretions: Evidence for episodic paleohydrogeologic methanogenesis. Geological Society of America Bulletin, 99, 385-394. http://dx.doi.org/10.1130/0016-7606(1987)99<385:TIACEO>2.0.CO;2

Sinninghe Damsté, J.S., Rijpstra, W.I.C., Schouten, S., Fuerst, J.A., Jetten, M.S.M. and Strous, M., 2004. The occurrence of hopanoids in planctomycetes: implications for the sedimentary biomarker record. Organic Geochemistry, 35, 561-566. http://dx.doi.org/10.1016/j.orggeochem.2004.01.013

Stern, G. and Wagreich, M., 2013. Provenance of the Upper Cretaceous to Eocene Gosau Group around and beneath the Vienna Basin (Austria and Slovakia). Swiss Journal of Geosciences, 106, 505-527. http://dx.doi.org/10.1007/s00015-013-0150-8

Strauss, P.E., Harzhauser, M., Hinsch, R. and Wagreich, M., 2006. Sequence Stratigraphy in a classic pull-apart basin (Neogene, Vienna Basin). A 3D seismic based integrated approach. Geologica Carpathica, 57, 185-197.

Talbot, H.M. and Farrimond, P., 2007. Bacterial populations recorded in diverse sedimentary biohopanoid distributions. Organic Geochemistry, 38, 1212-1225. http://dx.doi.org/10.1016/j.orggeochem.2007.04.006

Thomka, J.R. and Lewis, R.D., 2013. Siderite concretions in the Copan Crinoid Lagerstätte (Upper Pennsylvanian, Oklahoma): Implications for interpreting taphonomic and depositional processes in mudstone successions. Palaios, 28, 697-709. http://dx.doi.org/10.2110/palo.2012.p12-130r

Wagreich, M., 2001. Paleocene – Eocene paleogeography of the Northern Calcareous Alps (Gosau Group, Austria). In: Piller, W.E. and Rasser, M.W. (eds.), Paleogene of the Eastern Alps. Österreichische Akadademie der Wissenschaften, Schriftenreihe der Erdwissenschaftlichen Kommissionen, 14, 57-75.

Wagreich, M., Egger, H., Gebhardt, H., Mohammed, O., Spötl, C., Koukal, V. and Hobiger, G., 2011. A new expanded record of the Paleocene-Eocene transition in the Gosau Group of Gams (Eastern Alps, Austria). Annalen des Naturhistorischen Museums in Wien, 113, 35-65. http://www.jstor.org/stable/41701734

Wieninger, A., 2009. Kalk-Konkretionen aus der Sandgrube Steinbrunn/Bgld. Bachelor's thesis, Universität Wien, Vienna, Austria, 32 pp.

Wilkin, R.T. and Barnes, H.L., 1997. Formation processes of framboidal pyrite. Geochimica et Cosmochimica Acta, 61, 323-339. http://dx.doi.org/10.1016/S0016-7037(96)00320-1

Yli-Hemminki, P., Jørgensen, K.S. and Lehtoranta, J., 2014. Iron-manganese concretions sustaining microbial life in the Baltic Sea: The structure of the bacterial community and enrichments in metal-oxidizing conditions. Geomicrobiology Journal, 31, 263-275. http://dx.doi.org/10.1080/01490451.2013.819050

Zheng, Y.-F., 1999. Oxygen isotope fractionation in carbonate and sulfate minerals. Geochemical Journal, 33, 109-126. http://dx.doi.org/10.2343/geochemj.33.109

Ziegenbalg, S.B., Brunner, B., Rouchy, J.M., Birgel, D., Pierre, C., Böttcher, M.E., Caruso, A., Immenhauser, A. and Peckmann, J., 2010. Formation of secondary carbonates and native sulphur in sulphate-rich Messinian strata, Sicily. Sedimentary Geology, 227, 37-50. http://dx.doi.org/10.1016/j.sedgeo.2010.03.007

Ziegenbalg, S.B., Birgel, D., Hoffmann-Sell, L., Pierre, C., Rouchy, J.M. and Peckmann, J., 2012. Anaerobic oxidation of methane in hypersaline Messinian environments revealed by ^{13}C-depleted molecular fossils. Chemical Geology, 292-293, 140-148. http://dx.doi.org/10.1016/j.chemgeo.2011.11.024

Received: 23 November 2015
Accepted: 29 March 2016

Lydia M. F. BAUMANN[1),2)*)], Daniel BIRGEL[1)], Michael WAGREICH[2)] & Jörn PECKMANN[1),2)];

[1)] Institut für Geologie, Universität Hamburg, Bundesstraße 55, 20146 Hamburg, Germany;

[2)] Department für Geodynamik und Sedimentologie, Universität Wien, Althanstraße 14, 1090 Wien, Austria;

[*)] Corresponding author: lydia.baumann@uni-hamburg.de